

Modeling, Analysis and Experimental
Validation of a Three Degree of Freedom
Electromagnetic
Energy Harvester

by

Yan Chen

A thesis

presented to the University of Waterloo

in fulfillment of the

thesis requirement for the degree of

Master of Applied Science

in

Mechanical Engineering

Waterloo, Ontario, Canada, 2012

©Yan Chen 2012

Author's Declaration

I hereby declare that I am the sole author of this thesis. This is a true copy of the thesis, including any required final revisions, as accepted by my examiners.

I understand that my thesis may be made electronically available to the public.

Abstract

The objective of this thesis is to describe the modeling, analysis and experimental validation of a prototype three degree of freedom electromagnetic energy harvester. Furthermore, the thesis aims to demonstrate the performance improvement over a single degree of freedom (SDOF) design presented in the literature, when bifurcation in the system is not engaged.

Electro-mechanical models of the SDOF and multiple degree of freedom (MDOF) energy harvesters are developed to predict the frequency response functions of the systems. The models are implemented using MATLAB, and solved numerically using the ODE 45 function. The models consider the geometry of the system, the mechanical damping, the electrical damping, the magnetic repulsion force, the output peak displacements, and the peak load voltage of the energy harvesters.

Prototype SDOF and MDOF energy harvesters are built and tested under sinusoidal sweep excitation. The prototypes are mounted on an electromagnetic shaker via a test structure. The frequency response functions of the prototypes are measured when subjected to sinusoidal excitation from 4 to 16Hz. The displacement of the center magnet is measured using a laser displacement sensor, and the peak voltage is measured from the load circuit. The magnetic force and mechanical damping of the system are experimentally identified, and used as input parameters for the model.

The results of the experiments are compared to the model predictions for validation. The experimental results are in good agreement with model predictions. Furthermore, a study is presented to evaluate the effects of the spring stiffness in the MDOF harvester, and to find the optimal spring stiffness to maximize power generation. The results show a spring stiffness of 25N/m produced the highest average peak power. The average peak voltage is as much as 30% higher, over the frequency range 1-20 Hz when compared to the SDOF harvester under the same base excitation level. However, a more rigorous study is needed to determine the optimal spring stiffness because there is a tradeoff between increase volume and increase power production.

The MDOF harvester represents remarkable improvements over the SDOF harvester. To fully take advantage of the design, all three magnets should be used for energy harvesting. In the

present experiment, only the middle magnet is used for energy harvesting to provide a direct comparison to the SDOF design.

Acknowledgements

I would like to thank my supervisor, Dr. Armaghan Salehian for her technical guidance and unyielding support through my graduate studies.

To the technical staff at University of Waterloo, specifically Jorge Cruz who operates the material shop, Quoi, John and Mike who supervise the engineering machine shop, and Andy Barber. Your assistance was invaluable in the fabrication of the prototypes and the setup of test equipment.

In addition I would like to express my appreciation to the member of my workgroup especially Mohammed Ibrahim and Karim Moussa.

I would like to thank my mother who kept me focused and provided me with constant support through the whole process. Thank you to my friends who kept me motivated, and a special thanks to Peter Chu who greatly assisted me in editing of this thesis.

Finally, I would like thank the Province of Ontario for their financial support.

Dedication

To my mother, Jin Zou, who has always pushed me to succeed and supported me along the way.

Table of Contents

List of Figures	ix
List of Tables	xi
Nomenclature	xii
Chapter 1: Introduction	1
1.1 Background and Motivation	1
1.2 Thesis Organization	5
Chapter 2: Literature Review	7
2.1 Active Control Methods.....	7
2.2 Passive Methods.....	8
2.2.1 Frequency Up-Conversion	8
2.2.2 Non-linear Systems	9
2.3 Objectives and Scope	11
Chapter 3: Modeling	14
3.1 Description of Energy Harvesting System Configuration	14
3.2 Electromechanical Model for MDOF System	15
3.2.1 Electrical Component.....	15
3.2.2 Mechanical Component	16
3.3 Electromechanical Model for SDOF System.....	19
3.4 Characterization of Magnetic Flux Density using COMSOL.....	20
Chapter 4: Experimental Setup	23
4.1 Test Equipment and Sensors.....	23
4.1.1 Excitation Mechanism	24
4.1.2 Signal Generation, Sensing Mechanisms and Data Recorder.....	24
4.2 Prototype Design.....	26
4.2.1 Exterior Casing	27
4.2.2 Middle Magnet Assembly.....	28
4.2.3 End Magnet Assembly.....	29
4.2.4 Final Assembly	29

4.3 Test Structure	29
4.4 Experimental Procedure.....	30
4.5 Characterization of Magnetic Force.....	32
4.5.1 Test Setup.....	32
4.5.2 Test Procedure	33
4.5.3 Curve Fitting	34
4.6 Damping Characterization using Log Decrement Method.....	35
4.6.1 Damping Measurement Test Setup.....	35
4.6.2 Test Procedure	36
4.6.3 Curve Fitting	36
Chapter 5: Experimental Validation of the Developed Model	40
5.1 Numerical Results.....	40
5.2 Model Validation	45
5.3 Bifurcation	49
Chapter 6: Analysis of the Effect of Spring Stiffness.....	52
6.1 Simulation Assumptions and Procedure	52
6.2 Simulation Results	53
Chapter 7: Conclusion and Future Work	57
References.....	60
Appendix A: MDOF Model Code	64
Appendix B: SDOF Model Code.....	69
Appendix C: Magnet Datasheet	73
Appendix D: Component Datasheet	74
Keyence IL-100 CMOS Analog Laser Sensor.....	74
Dytran 3035AG Accelerometer	75
Modal Shop 2075E Dual Purpose Shaker.....	76
Chatillon DFX II Digital Force Gauge	77
Appendix E: Additional Experiment Images.....	78

List of Figures

Figure 1 – Power Density vs. Voltage graph of different energy sources courtesy of Kimberly Cook-Chennault [1]	1
Figure 2 - Schematic of a tunable energy harvester using magnetic force courtesy of Dibin Zhu [16].....	7
Figure 3 – Schematic of the frequency up-conversion mechanism courtesy of Ibrahim Sari [11]	9
Figure 4 – Schematic of a piezomagnetoelastic energy harvester courtesy of Alper Erturk [19]	10
Figure 5 – Schematic of a levitated magnet energy harvester	11
Figure 6 - Schematic of the harvester units: SDOF (left) and MDOF (right).....	14
Figure 7 – Diagram of the electric circuit used in the experiment.....	16
Figure 8 – Free body diagrams of the MDOF harvester a) top b) middle and c) bottom magnets respectively	17
Figure 9 - Free body diagrams of the SDOF harvester’s middle magnet	19
Figure 10 - Magnetic flux density of an 1 inch ring magnet using an 2D axial symmetric COMSOL simulation	20
Figure 11 - Average radial flux obtained from the COMSOL simulation fitted to a sum of sine equation.....	21
Figure 12 - Experimental setup.....	23
Figure 13 - Schematic diagram of the SCADAS Mobile internal architecture [33].....	25
Figure 14 – Prototype energy harvesters: SDOF (left) and MDOF (right).....	27
Figure 15 –Exterior casings: SDOF (top) and MDOF (bottom).....	28
Figure 16 - Middle magnet assemblies: SDOF (top) and MDOF (bottom).....	28
Figure 17 – End magnet assemblies: SDOF (left) and MDOF (right).....	29
Figure 18 – Magnetic force characterization test setup	33
Figure 19 – Magnetic repulsion force data plotted with the curve fit.....	34
Figure 20 – SDOF middle magnet damping data with the curve fit.....	37
Figure 21 - MDOF middle magnet damping data with the curve fit	37
Figure 22 - MDOF end magnet damping data with the curve fit.....	38
Figure 23 – Peak displacement vs. frequency graph by the model for the SDOF harvester at 0.35g (top) and 0.5g (bottom).....	41

Figure 24 - Peak voltage vs. frequency graph by the model for the SDOF harvester at 0.35g (top) and 0.5g (bottom).....	42
Figure 25 -Peak displacement vs. frequency graph by the model for the top, middle, and bottom magnets of the MDOF harvester at 0.35g.....	43
Figure 26 - Peak displacement vs. frequency graph by the model for the top, middle, and bottom magnets of the MODF harvester at 0.5g.....	44
Figure 27 - Peak voltage vs. frequency graph by the model for the middle magnet of the MODF harvester at 0.35g (top) and 0.5g (bottom)	44
Figure 28 - Peak displacement comparison between the experimental results and the model for the SDOF harvester at 0.35g (top) and 0.5g (bottom)	46
Figure 29 - Peak voltage comparison between the experimental results and the model for the SDOF harvester at 0.35g (top) and 0.5g (bottom)	46
Figure 30 – Sample base excitation acceleration data recorded by the accelerometer with a target value of 0.5g.....	47
Figure 31 - Peak displacement comparison between the experimental results and the model for the middle magnet of the MDOF harvester at 0.35g (top) and 0.5g (bottom).....	47
Figure 32 - Peak voltage comparison between the experimental results and the model for the middle magnet of the MDOF harvester at 0.35g (top) and 0.5g (bottom).....	48
Figure 33 – Peak displacement vs. frequency graph by the model for the SDOF harvester at 1.2g	50
Figure 34 – Peak displacement vs. frequency graph by the model for the top, middle, and bottom magnets of the MODF harvester at 1.2g.....	50
Figure 35 - Model peak voltage frequency response functions with different spring stiffness at 0.35g.....	54
Figure 36 - Average peak voltage over the frequency spectrum (1-20Hz) for different spring stiffness at 0.35g	54
Figure 37 - Model peak voltage frequency response functions with different spring stiffness at 0.5g.....	55
Figure 38 - Average peak voltage over the frequency spectrum (1-20Hz) for different spring stiffness at 0.5g	55

List of Tables

Table 1 - Table of the coefficients for average radial flux curve fit	21
Table 2 – Table of the sine sweep parameters	32
Table 3 – Table of the damping test data	39
Table 4 – Parameter values measured for SDOF and MDOF harvesters	40
Table 5 – Parameter values used in the simulation for the SDOF and MDOF harvesters.	53

Nomenclature

\vec{A}	cross sectional area vector
b	base displacement
\dot{b}	base velocity
\ddot{b}	base acceleration
\vec{B}	flux density
B_r	remanence
B_{rad}	radial flux density
$B_{rad, avg}$	average radial flux density
c_e	electrical damping coefficient
c_m	mechanical damping coefficient
c_{tot}	total damping coefficient $c_{tot} = c_m + c_e$
DAS	data acquisition system
F_b	force between bottom and middle magnet
F_t	force between top and middle magnet
FEA	finite element analysis
g	gravitational constant [$g=9.81m/s^2$]
H	magnetic field strength
h_i	height of magnet i
i	electrical current
K	electrodynamics coupling coefficient
k_i	spring stiffness of i
L_m	length of MDOF energy harvester
L_s	length of SDOF energy harvester
LS_i	free length of spring of i
\vec{l}	loop vector of the coil
l_{coil}	total length of the coil
M	coercive force
MDOF	multiple degree of freedom
MEMS	microelectromechanical systems

m_i	mass of i
N	number of coil turn
NdFeB	neodymium
R_{coil}	coil resistance
R_{load}	load resistance
SDOF	single degree of freedom
V	voltage
\vec{v}	relative velocity vector
x_i	absolute displacement of i
\dot{x}_i	absolute velocity of i
\ddot{x}_i	absolute acceleration of i
z_i	relative displacement of i
\dot{z}_i	relative velocity of i
\ddot{z}_i	relative acceleration of i
μ_0	permeability of free space [$\mu_0 = 4\pi \times 10^{-7} \text{ N/A}^2$]
ζ	damping ratio
ω_d	damped natural frequency
ω_n	undamped natural frequency
ϕ	phase shift
Φ	magnetic flux

Chapter 1: Introduction

1.1 Background and Motivation

Energy harvesting refers to capturing energy available in the environment and converting it to a useful form of energy such as electricity. Current forms of energy harvesting employ wind, solar, mechanical/vibration, thermal, and radio waves. Wind and solar energy harvesting techniques are the most prominent and established because they are abundant resources in the environment. Capturing wind and solar energy can produce higher power density when compared with other energy harvesting techniques. While other methods may harvest orders of magnitude less energy, they have other advantages over wind and solar. One the advantages is the ability to harvest energy in imbedded applications (where the energy harvester is placed in an enclose area) using thermal or vibrations. The harvester has no access to the outside environment and is unable to capture energies such as wind and solar. These methods have been the focus of research in recent years. Figure 1 shows of a comparison of power and voltage production of different power sources.

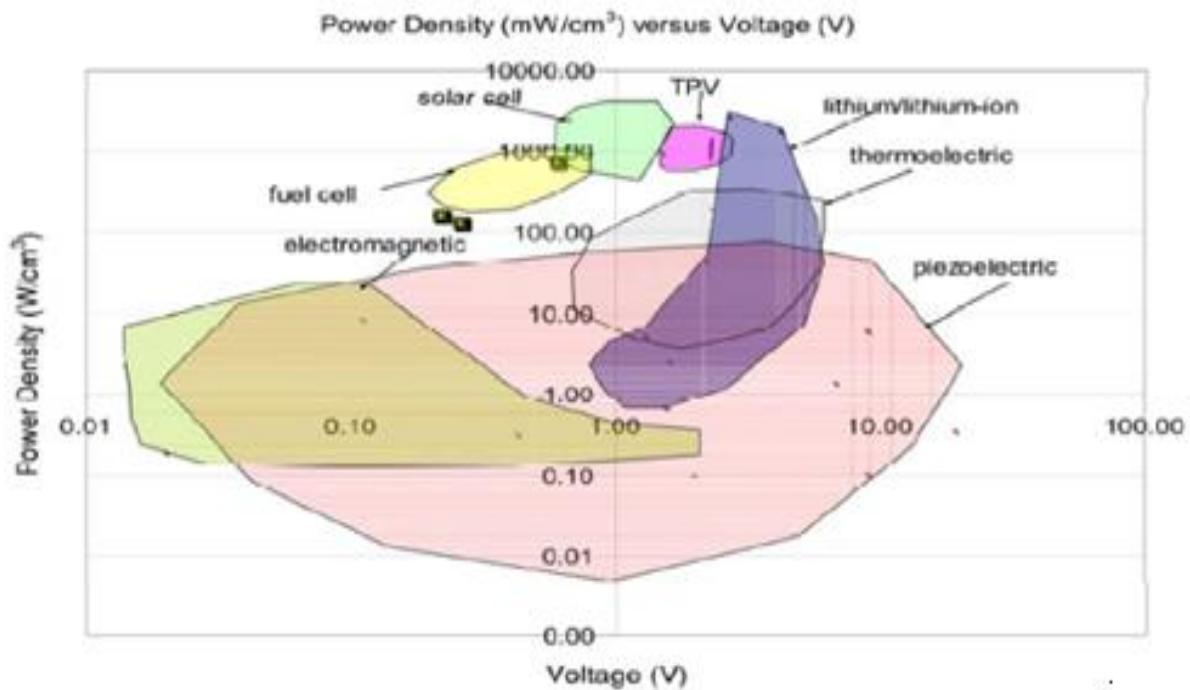


Figure 1 – Power Density vs. Voltage graph of different energy sources courtesy of Kimberly Cook-Chennault [1]

With the increase usage of miniature wireless electronics, vibration based energy harvesting systems can be an enabling technology and an attractive option as a power source. Vibration energy is abundant in the ambient environment. Unlike other forms of energy harvesting, vibration energy does not require direct access to the environment such as wind and solar. It can operate in enclosed locations. This characteristic can be an enormous advantage. In addition, new miniature electronics have low power consumption requirements, in the order of milli-watts. Researchers have successfully demonstrated the use of vibration energy harvesting systems to power miniature wireless electronic devices [2, 3]. Roundy and Wright [2] demonstrated energy harvesting system as the power source for a custom design radio transmitter. Torah et al [3] advanced a step further. They designed and fabricated an integrated autonomous wireless condition monitoring sensor system. The sensor package includes a vibration based energy harvester, a capacitor, an accelerometer, a transmitter and an onboard controller. Their energy harvester charges a capacitor. When the capacitor is fully charged, an onboard controller activates the accelerometer and the reading is transmitted. Then the sensor is put back to sleep mode. The complete cycle takes 65 micro joules [3].

The two main methods for converting vibrations energy to electrical energy are piezoelectricity and electromagnetic induction.

Electromagnetic induction is based on Faraday's law of induction [4], which states an electromotive force or, voltage (V) is generated when there is a time-varying flux, (ϕ) acting through a number of coils (N).

$$V = -N \frac{d\phi}{dt} \quad (1)$$

Electromagnetic energy harvesting systems utilize vibration to create a relative motion between a permanent magnet and the conducting coils. The relative movement caused by mechanical vibration between the magnet and the conducting coil is the main component for generating a time varying flux in the coils.

Piezoelectricity is a characteristic exhibited by materials with electromechanical coupling where any strain in the material produces a charge. This energy conversion occurs because the piezoelectric molecular structure is oriented such that the material exhibits a local charge

separation known as an electric dipole. When strain energy from mechanical vibration, is applied to the material, a deformation of the dipole occurs and the formation of a charge can be removed from the material and used to power various devices [5]. In the reverse piezo-effect, the application of an electric field results in stress and strain in the piezoelectric material.

Each of the two transduction methods has its own merits. One study [6] has shown electromagnetic induction is capable of higher power density compared to piezoelectricity when normalized with the input vibration level. Piezoelectric and electromagnetic energy harvesters in the literature are compared using their stated volume, vibration input level and power generation. The normalized power density can be much greater for electromagnetic energy harvesters. In particular, electromagnetic induction is popular in macro scale applications due to their ease of fabrication. This method has been used for creating energy generating automotive shock absorbers [7, 8]. The energy generated in passive mode can be used to control the dynamics of the vehicle in active mode, reducing the overall energy requirement of the shock absorber. Other examples of energy harvester using electromagnetic induction can be found [9]. An electromagnetic energy harvester can be made about the size of an AA battery, facilitating the transition from battery to energy harvesting devices as a power source.

Piezoelectric energy harvesting systems are capable of generating much higher voltages compared with electromagnetic energy harvesting systems as seen in Figure 1. Higher voltages, greater than about 0.2V, are desirable to allow for the use of passive rectification from AC voltage to DC voltage without reducing efficiency [4]. This method is prevalent in micro scale applications due to its compatibility with micro fabrication techniques. A good number of studies [10, 11] pertaining to piezoelectric material use a cantilever beam design. Cantilever beams can be fabricated using current micro-machining techniques such as etching. A piezoelectric material can then be applied to the cantilever beam using deposition; hence the reason piezoelectric transduction method is most common in Microelectromechanical Systems (MEMS). As mentioned previously, vibration causes the cantilever beam to deflect, and produce strain, and as a result the piezoelectric material is able to directly convert the applied strain into electricity. Conversely, the application of the electromagnetic induction method is difficult in MEMS because multiple-turn coil fabrication is challenging with current MEMS fabrication

techniques [11]. Similar works based on cantilever-based piezoelectric energy harvesters are shown in [12, 13]

Hybrid energy harvesting techniques are possible when both transduction methods are applied together. The cantilever configuration is the most popular for this method where a magnet can be added to the tip of the piezo-cantilever. Electricity is then generated by electromagnetic induction as the magnet moves relative to a fixed coil during vibration in addition to those generated by the piezoelectric material applied on the cantilever beam [14, 15]. Although hybrid energy harvesters are an intriguing method to generate additional power, the vastly different voltages generated by different transduction methods pose energy storage and recovery challenges.

In summary, the piezoelectric transduction method is well suited to micro scale application due to its compatibility with MEMS fabrication techniques. In macro scale applications, the electromagnetic induction method is superior due to its much higher normalized power density compared with piezoelectric transduction method, which indicates it would have a higher performance in low vibration levels. Coil fabrication is simple and inexpensive. Magnets with strong magnetic fields such as Neodymium (NdFeB) are widely available and relatively inexpensive. High voltages can be generated by selecting the appropriate magnet and coil design.

In most vibration based energy harvesting techniques, the concept of resonance is employed. Resonance occurs when the input frequency of vibration matches the natural frequency of the energy harvester, resulting in large amplitude vibration. The main disadvantage of the current generation of energy harvester is its sensitivity to vibration input frequency and its narrow bandwidth. The power output drops dramatically when the input frequency is shifted away from the natural frequency of the system, thus high energy output is difficult to sustain. In addition, a constant input frequency does not often occur in real-world applications. Input frequency is often variant and dynamic due to any number of factors the user is unable to control. Such deficiency has been the focus of many researchers. Their strategies and results are discussed in the subsequent sections.

1.2 Thesis Organization

So far, a general overview of the concept of energy harvesting is provided. The goal of this thesis is to detail the analysis and experimental investigation of a multiple degree of freedom (MDOF) energy harvester. The objective is to develop a model to predict the frequency response function of the energy harvester and evaluate its performance against existing designs. The rest of the thesis is organized as follows:

Chapter 2 reviews the literature on energy harvesting designs and their implementation to overcome the narrow frequency of operation, a challenge faced by many energy harvesting systems. This chapter focuses on active control systems (where the natural frequency can be altered), frequency up-conversion technique and non-linear systems. Performance comparison is drawn between different designs. The specific objective of this thesis is also outlined in this chapter

Chapter 3 provides a detailed description of a multiple degree of freedom electromagnetic energy harvesting system. A mechanical model of the system is derived and the resulting coupled multiple MDOF equation is solved numerically. An electromagnetic model is also presented and combined with the mechanical model to predict the energy harvesting performance of the system.

Chapter 4 provides a detailed description of experimental setups. The detail for the design and fabrication of the prototype and experimental procedures are outlined. Parameters required by the model such as magnetic force and mechanical damping are obtained experimentally.

Chapter 5 provides results based on the parameters experimentally obtained in the previous chapter. The results from the model are compared to with the experimental results obtained using methods outlined in Chapter 4. Observations made regarding the performance of the energy harvesters and discrepancies between model and experimental results are noted.

In Chapter 6, the performance of single degree and three degree of freedom energy harvesting system is analyzed. Observation and comparison are made using simulation results. Energy production over the frequency range from 1 to 20 Hz is maximized by finding the optimum stiffness of the springs.

Finally, the thesis concludes with the design and performance of the three degree of freedom energy harvesting design. Future on optimization of stiffness based on total power generation using all three mass and miniaturization of the prototype are discussed.

Chapter 2: Literature Review

This chapter focuses on research to overcome the narrow frequency range of operation in energy harvesting designs. Specifically, the methodology can be divided into two categories, active control methods and passive methods. Active control methods involve matching the energy harvester's natural frequency with the ambient input vibration frequency. Passive systems exploit other favorable characteristics such as bifurcation in non-linear systems, material properties and energy transfer mechanisms in the frequency up-conversion technique.

2.1 Active Control Methods

Active control methods operate on the principle of altering the system's natural frequency to match the input vibration frequency. Thus, it is able to continuously operate at the peak power output. The natural frequency is altered by changing the spring stiffness of the system. Different methods of changing the spring stiffness have been proposed and are outlined below.

In Zhu et al [16], a pair of magnets is used to apply an axial compressive force to a cantilever beam. One magnet is fixed to the free end of the cantilever beam, while the position of the other magnet can be varied using a linear actuator as seen in Figure 2. The amount of applied axial force is a function of distance between two magnets. Therefore, an increase in the applied axial force will result in an increase in the spring stiffness of the beam. Thus, a corresponding increase in the natural frequency of the system is achieved. This is analogous to tightening a guitar string to play a higher note.

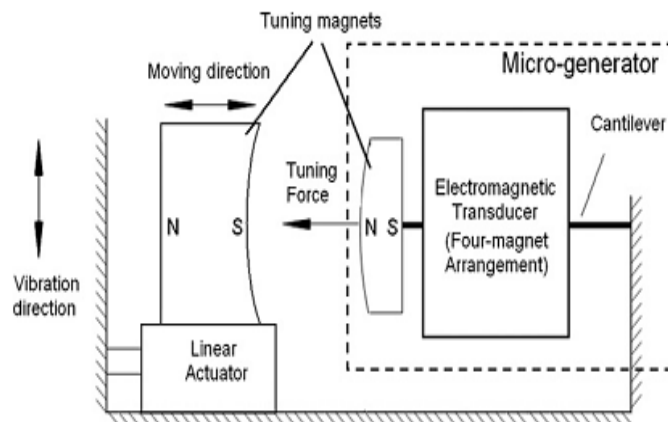


Figure 2 - Schematic of a tunable energy harvester using magnetic force courtesy of Dibin Zhu [16]

In another study [17], the cantilever beam is constructed consisting of a polymer beam sandwiched between piezoelectric plates. Using the previously mentioned inverse piezoelectric effect, a charge is applied to the piezoelectric material to change the stiffness of the beam. The magnitude of the change in the stiffness is a function of the charge. The charge effect diminishes over time and reapplication is required to maintain the stiffness of the beam. One benefit of this design is that the piezoelectric material is used as a tuning device (to change the natural frequency of the energy harvester) as well as a harvesting energy system.

The primary benefit of the active control method is the continual operation at maximum energy output. However, its main disadvantage is the power requirement of an active control system. This aspect is not part of the scope of either study outlined above. The required control system has not been developed and the energy requirement of the tuning mechanism is not known. The control system and the control mechanism also add complexities, which detracts from the benefit of this type of system. The overall effectiveness of this type of system has not been explored.

2.2 Passive Methods

2.2.1 Frequency Up-Conversion

Frequency up-conversion is a passive method with which researchers have experimented to create broadband energy harvesters. This type of device decouples the ambient input frequency from the internal operation frequency. Mechanical energy causes one degree of freedom the device to vibrate at the frequency of the input vibration. The energy from the vibration from the first degree of freedom is transferred to a second degree of freedom. This second degree of freedom, which is used for energy production, is allowed to vibrate freely at a much higher frequency than the input vibration.

For example, in one study [11], Sari et al fabricated a MEMS device with a polymer diaphragm. The diaphragm can be excited with a wide range of input vibration frequency, from 70 to 150 Hz. A magnet is attached to the bottom of the diaphragm. It latches on to the tips of an array of cantilever beams when the diaphragm is moving downward, as seen in Figure 3. Then, the magnet releases the tips when the diaphragm returns upward, giving the beams some initial displacement. The beams are then able to freely vibrate at their own natural frequency, and

produce electrical energy. The beams' natural frequencies are much higher than the input frequencies.

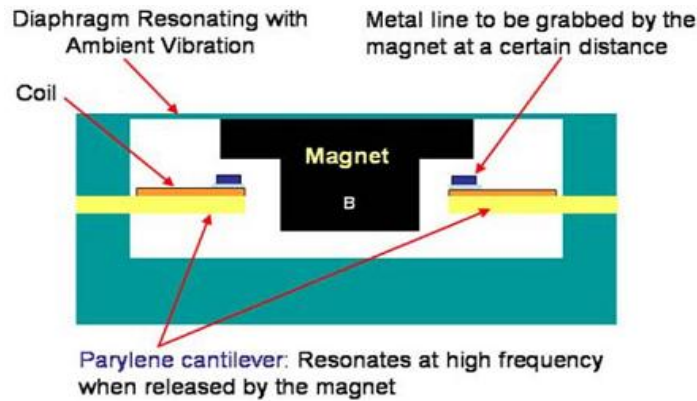


Figure 3 – Schematic of the frequency up-conversion mechanism courtesy of Ibrahim Sari [11]

The main benefit of the frequency up-conversion technique when compared to the active control method is that it is a passive system. Thus, it does not have the added complexity and power consumption due to an active control system. A significant challenge is increasing the efficiency of the energy transferring mechanism. Although the prototype is a MEMS device, the power generated is very small, in the order of nano-watts [11].

2.2.2 Non-linear Systems

Non-linear systems characteristics such as bifurcation can be exploited for broadband energy harvesting. In some systems, this behavior is characterized by the addition of a cubic displacement term and it is best described by the Duffing equation [18]. Often, non-linearity is introduced into the system using magnetic forces, given that it is not proportional with respect to distance. Different configurations have been proposed.

In Erturk and Inman [19], two permanent magnets are placed on either side of a cantilever beam as seen in Figure 4. The cantilever beam is created with a bimorph of piezoelectric and ferromagnetic material. The permanent magnets are attracted to the ferromagnetic beam, creating two stable equilibrium positions on either side and an unstable equilibrium position in the center, known as a double well system or bi-stable snap-through mechanism. This configuration is known as the Moon beam, after Francis Moon who first described this system [18]. A similar configuration uses two permanent magnets in repulsion. One magnet is placed on the tip of the cantilever beam while the other magnet is placed directly in front of the first

magnet. This configuration, although not the same as the original Moon beam, can have the same effect [20, 21]. Under constant amplitude excitation at low frequencies, the beam vibrates about one of the stable equilibrium points at low amplitudes. As the amplitude of the excitation increases, more energy is added to the system. At a certain point, the system gains enough energy and the beam crosses the center position. It vibrates from one stable equilibrium point to the other stable equilibrium point, resulting in large amplitudes of vibration. The study [19] shows that large amplitudes of vibrations can also be created with low input excitation levels. In this case, an impulse is applied to supply the necessary initial energy needed to transverse from one equilibrium position to the next. In addition, the study demonstrates the large amplitude vibration can be sustained over the frequency range from 5 to 8 Hz. However, the vibration frequency is kept constant for each individual test, so it is uncertain if large amplitude vibration can be sustain under varying input frequencies.

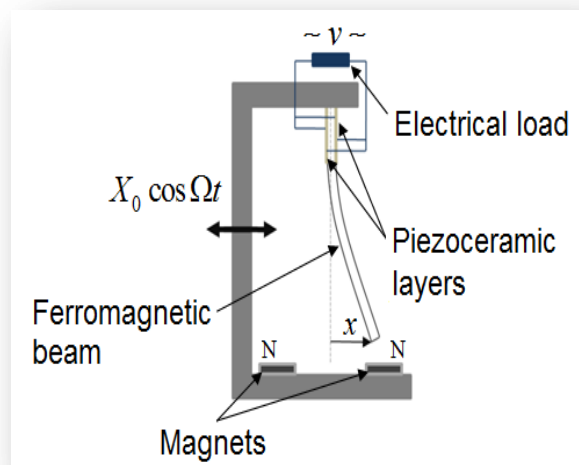


Figure 4 – Schematic of a piezomagnetoelastic energy harvester courtesy of Alper Erturk [19]

In other studies [22-24], two fixed magnets levitate a third magnet positioned in between them using repulsive magnetic force as seen in Figure 5. This type of system can be described as a mono-stable spring hardening system. Due to this non-linear stiffness, the magnetic force is best modeled as a higher-order polynomial function with respect to displacement, usually cubic. Mann and Sim [22] and Saha et al [24], show for small displacement, the system behaves much like a linear system. The non-linearity is only evident for larger amplitudes of vibration.

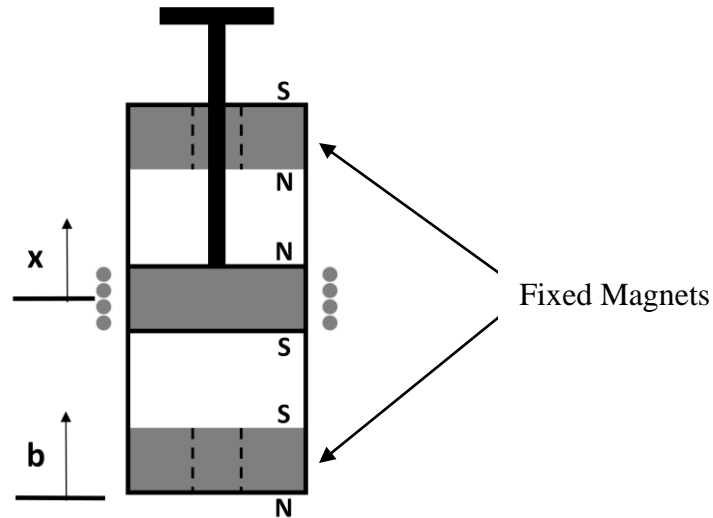


Figure 5 – Schematic of a levitated magnet energy harvester

Lee et al. [23] show when the energy harvester (Figure 5) is subjected to a sinusoidal sweep from low to high frequencies, the power production increases almost linearly, with respect to frequency, once it passes a frequency threshold. In addition, a non-linear system can have similar peak power performance when compared to linear systems, but they occur at different frequencies. However, non-linear systems have multiple solutions. The large amplitude vibration experience by the energy harvester only occurs when the sinusoidal sweep is from low to a high frequency. When the sweep is from high to low frequencies, the power generated is much lower. This is a characteristic of bifurcation.

For broadband energy harvesting using non-linear energy harvester, large amplitudes of vibration must be generated and sustained. This creates severe restrictions on the vibration source. For the snap-through mechanism, the level of excitation in the system is important. Its response to varying frequency of vibration such as random vibration or sinusoidal sweep is not known. For the levitated magnet energy harvester, the level of excitation and the direction of frequency change are important. These restrictions limit the applications of these designs.

2.3 Objectives and Scope

In summary, all methodologies reviewed and presented above have their own merits. There are no clear cut winners. Each method faces challenges that must be overcome in order to be successful. A complete review of the methodologies used for broadband energy harvesting is

contained in [25]. Increasing the operating frequency range of energy harvesting system is still a problem that must be resolved.

This thesis presents an alternative three degree of freedom energy harvesting configuration (hereon refer to as MDOF energy harvester) for investigation. The proposed configuration is a modification of a configuration used by Mann and Sim [22], Lee et al [23], and Saha et al [24].

The main objectives of this thesis are the following [26]:

- Describe the development of a numerical model for the proposed MDOF energy harvester and a SDOF energy harvester
- Detailed design, fabrication, and testing of prototypes of energy harvester to evaluate the results of the model
- Using the numerical model, analyze the proposed design's performance for low frequency vibrations.

The goal of this research is to develop a passive MDOF energy harvester for use in low frequency vibration applications. Due to the frequencies of interest, macro-scale energy harvester is most suitable for this application. Thus, electromagnetic induction is the most logical transduction method because of its higher normalized power density and its simple fabrication as mentioned previously. The goal of the MDOF design is to improve the power production of the energy harvester over a wide range of frequencies when compared to the SDOF design.

One possible application for low frequency vibration energy harvester is capturing energy from human motion ranging from 1 to 20Hz range. Saha et al has designed electromagnetic energy harvesters with peak response at 6.5Hz and 8 Hz to harvest energy from human motion [24]. Acceleration level with peak amplitudes of 0.5g and 1g with corresponding frequencies of 2Hz and 2.75Hz are recorded inside a backpack carried by a person while walking and slow jog respectively [24]. Another study [27] using electromagnetic energy harvester in the sole of a shoe to harvest energy found that 5 Hz approximately corresponds to the walking speed of two steps per second. Commercial energy harvesting devices are also available for charging portable electronics from companies such as nPower PEG [28].

Another possible application is in structural health monitoring. Low frequency vibrations exist in large structures. Galchev et al [29] found that vibrations with frequencies ranging from 2 to 30 Hz and up to 0.05g are available in bridges. For one particular bridge (RT11) in Potsdam, New York, the frequency associated with highest input power level is 3.1Hz [30]. The purpose of the low frequency energy harvester is to provide perpetual power for embedded sensors in these structures. Another possible application is use in automobiles. An energy harvester can be attached to the chassis of a car to power on-board sensors.

The scope of this work is limited to proving the merit of the proposed MDOF energy harvester. Sinusoidal sweep will be performed to find the frequency response functions of the energy harvesters. For the proposed MDOF energy harvester, only the middle magnet is used for energy harvesting, such that it provides a direct comparison to the SDOF energy harvester. Lastly, an analysis is performed to study the effect of the spring stiffness in the MDOF design.

In this chapter, energy harvesters with broadband application from literature are presented. The specific objective of this thesis is outlined above. The next step is to develop a model to find the frequency response functions of the proposed MDOF energy harvester.

Chapter 3: Modeling

In this chapter, an electromechanical model is developed for both the SDOF presented in literature and proposed MDOF energy harvester. First the electrical and mechanical coupling effect is analyzed. Then, the equations of the system are formulated using Newtonian laws. Lastly, a finite element analysis (FEA) is performed to obtain magnetic flux data required by the model.

3.1 Description of Energy Harvesting System Configuration

The SDOF energy harvester, shown in Figure 6, is similar to the configuration proposed by Mann and Sim [22], Lee et al [23] and Saha et al [24]. In this configuration, the top and bottom magnets are rigidly attached to the enclosure. In the proposed MDOF system, also shown in Figure 6, two springs are added to the top and bottom magnets, introducing two extra degrees of freedom. In the MDOF system, the top and bottom magnets are no longer fixed with respect to the enclosure, but are free to vibrate. The middle magnet remains levitated using the magnetic repulsion force of the top and bottom magnets. Electromagnetic induction is transduction method used because of its superior normalize power density performance and relative simple fabrication. In both systems, a coil is used to harvest energy from the central levitated magnet.

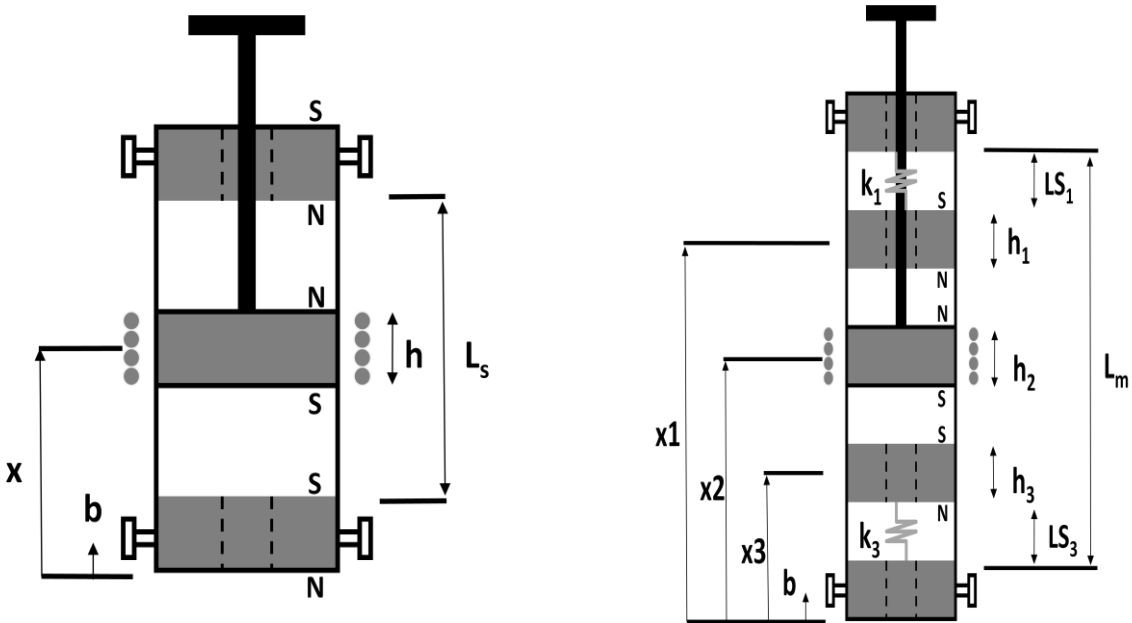


Figure 6 - Schematic of the harvester units: SDOF (left) and MDOF (right)

3.2 Electromechanical Model for MDOF System

3.2.1 Electrical Component

Electromagnetic induction is governed by Faraday's law (Eq. 1). There are two methods of generating a time varying flux to produce a voltage difference due to electromotive force (EMF): 1) the magnetic flux density, B varying in time or 2) a relative motion between the conducting coil and the permanent magnet. The two induction methods can be classified as induced voltage and motional voltage [31].

$$V_{emf} = V_{in} + V_{mo} = - \int_A \frac{\partial \vec{B}}{\partial t} d\vec{A} + \oint_l (\vec{v} \times \vec{B}) d\vec{l} \quad (2)$$

\vec{B} , \vec{v} , \vec{A} , \vec{l} are magnetic flux density, between the coil and the middle magnet, the cross sectional area vector and loop vector of the coil respectively. Applying Eq.2 to cylindrical coordinate of the proposed energy harvester results in a simplified equation (Eq. 3):

$$V_{emf} = v \left(-\frac{\partial B_x}{\partial h} S + B_{rad} l \right) \quad (3)$$

where B_x , B_{rad} , S and l are the magnetic flux density in the x -direction, the magnetic flux density in the radial direction, magnitudes of the coil area and perimeter respectively. The values of v , S and l are all positive. The detailed derivation of this equation can be found in Wang et al [31].

For an axially magnetized cylindrical magnet, the induced voltage is relatively small when compared to the motional voltage and does not contribute significantly to the overall power generated [31]. Thus, the induced voltage component is ignored.

Therefore the electromagnetic model further simplifies to Eq. 4.

$$V_{emf} = B_{rad,avg} l_{coil} v = K v \quad (4)$$

Here, $B_{rad,avg}$, l_{coil} , v , are the average radial flux density across the coil, the total length of the coil, and the relative velocity between the coil and the magnet. In this equation, the proportionality constant $K = B_{rad,avg} l_{coil}$, is called the electrodynamic coupling coefficient. Eq. 4 is also used by Cheng et al [32] & Lee et al [23].

The voltage generated by the energy harvester can be used to power a load circuit by connecting it to the two ends of the coil. For the purpose of this research, a simple load circuit shown in Figure 7 is used.

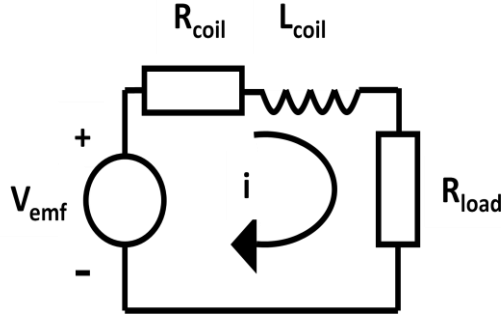


Figure 7 – Diagram of the electric circuit used in the experiment

The circuit consists of the voltage generated by the energy harvester, V_{emf} , the inductance and resistance of the coil, L_{coil} and R_{coil} respectively, and an external load, R_{load} , represented by a resistor.

The electrical equation can be derived by applying Kirchoff's law to the electrical circuit. Note that the inductance of the coil is neglected. The inductance of the coil is small, in the order of milli-Henry, which is small enough to be ignored [23].

$$(R_{coil} + R_{load})i = V_{emf} = Kv \quad (5)$$

In addition, the energy removed from the system in the form of electricity is equal to the force generated by the coil opposing the movement of the magnet (Eq. 6),

$$F_e = Ki \quad (6)$$

where F_e is the force opposing the movement of the magnet, and i is the electrical current.

3.2.2 Mechanical Component

The energy harvester is modeled with three discrete masses represented by m_1 , m_2 , and m_3 , for the top, middle, and bottom magnet respectively. The displacements of the magnets are defined by the displacement coordinates $x_1(t)$, $x_2(t)$, and $x_3(t)$. These displacement coordinates are with respect to the same ground reference. Attached to the top and bottom magnets are springs with constant stiffness k_1 and k_3 . The magnetic repulsion force between the top and middle mass is

represented by $F_t(x_1, x_2)$. Likewise, the repulsion force between the bottom and middle magnet is represented by $F_b(x_2, x_3)$. The mechanical energy dissipated in the system is modeled using viscous dampers with damping coefficients c_{1m} , c_{2m} , and c_{3m} . The electrical energy produced due to dissipation is then modeled by the mechanical force generated by the conducting coil [23, 32]. The structure is excited by a sinusoidal base displacement, $b(t)$, and it has the same reference point as the displacements coordinates as shown in Figure 6. Free body diagrams of the MDOF model are shown in Figure 8.

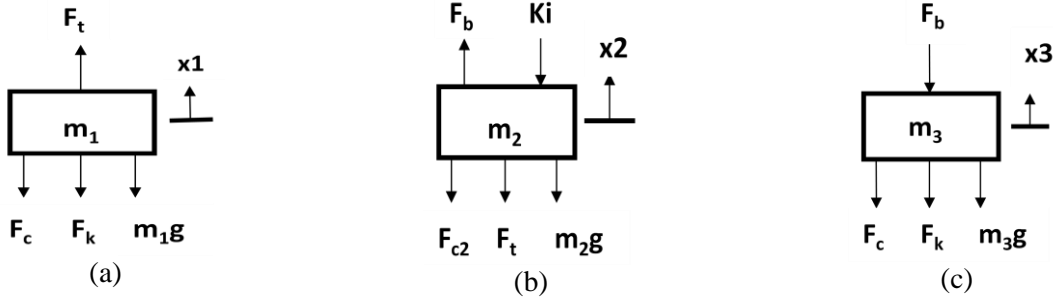


Figure 8 – Free body diagrams of the MDOF harvester a) top b) middle and c) bottom magnets respectively

Newton's second law is applied to formulate the equations of motion for the system. The dynamic equations of motion are given by Eq. 7 [26].

$$\begin{aligned}
 m_1 \ddot{x}_1 &= k_1 \left(b + L_m - LS_1 - \frac{h_1}{2} - x_1 \right) + c_{1m}(\dot{b} - \dot{x}_1) + F_t - m_1 g \\
 m_2 \ddot{x}_2 &= c_{1m}(\dot{b} - \dot{x}_2) - F_t + F_b - m_2 g - Ki \\
 m_3 \ddot{x}_3 &= k_3 \left(b + LS_3 + \frac{h_3}{2} - x_3 \right) + c_{1m}(\dot{b} - \dot{x}_3) - F_b - m_3 g
 \end{aligned} \tag{7}$$

At this point, all the displacement coordinates $x_1(t)$, $x_2(t)$, and $x_3(t)$ are with respect to ground. Since the relative velocities with respect to the moving base $b(t)$ are important for voltage calculations, a change of coordinate, $z_i = x_i - b$ is made to Eq. 7. Here, the subscript i denotes the number of the equation. Thus, the governing equations can be written in terms of relative displacements between the magnets and the exterior casing. In addition, rearranging Eq. 5 and Eq. 6, the force acting on the magnet due to the electromagnetic induction can be modeled as damping. The electrical damping coefficient c_{2e} , can then be found using Eq. 8.

$$c_e = \frac{K^2}{(R_{coil} + R_{load})} \tag{8}$$

The total damping on the middle magnet is then $c_{2tot}=c_{2m}+c_{2e}$, which is the summation of the mechanical and electrical damping. The mechanical damping is assumed to be constant and is obtained using experiment as outlined in Chapter 4. The resulting equations are presented in Eq. 9.

$$\begin{aligned}\ddot{z}_1 &= \frac{k_1}{m_1} \left(L_m + LS_1 - \frac{h_1}{2} - z_1 \right) + \frac{c_{1m}}{m_1} (-\dot{z}_1) + \frac{F_t}{m_1} - g - \ddot{b} \\ \ddot{z}_2 &= \frac{c_{2tot}}{m_2} (-\dot{z}_2) + \frac{F_b - F_t}{m_2} - g - \ddot{b} \\ \ddot{z}_3 &= \frac{k_3}{m_3} \left(LS_3 + \frac{h_3}{2} - z_3 \right) + \frac{c_{3m}}{m_3} (-\dot{z}_3) - \frac{F_b}{m_3} - g - \ddot{b}\end{aligned}\quad (9)$$

The base sinusoidal excitation is represented by:

$$b = -A \sin(\omega t) \quad (10)$$

Sinusoidal sweeps are performed during testing and the frequency of the base excitation ω changes accordingly. Therefore, the base velocity and acceleration are:

$$\dot{b} = A\omega \cos(\omega t) \quad (11)$$

$$\ddot{b} = -A\omega^2 \sin(\omega t) \quad (12)$$

where A is the amplitude of the base excitation.

The non-linear restoring forces $F_t(z_1, z_2)$ and $F_b(z_2, z_3)$ are presented in Eq. 13 and Eq. 14. The coefficients are determined through experiments, which is presented in Chapter 4.

$$F_t = ae^{b(z_1 - z_2 - (\frac{h_1 + h_2}{2}))} + ce^{d(z_1 - z_2 - (\frac{h_1 + h_2}{2}))} \quad (13)$$

$$F_b = ae^{b(z_2 - z_3 - (\frac{h_2 + h_3}{2}))} + ce^{d(z_2 - z_3 - (\frac{h_2 + h_3}{2}))} \quad (14)$$

The derived equations of motion are solved numerically using the ODE45 function in MATLAB. The MATLAB code can be found in Appendix A.

3.3 Electromechanical Model for SDOF System

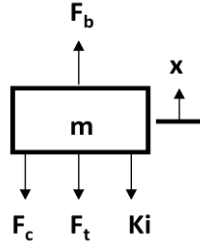


Figure 9 - Free body diagrams of the SDOF harvester's middle magnet

Similar to the case of the MDOF system, the equation of motion for the SDOF energy harvester is derived from the free body diagram shown in Figure 9. The displacement of the middle magnet is denoted by x , and is measured with respect to a fixed frame. The total mass of the magnet including the protruding rod is defined as m . The forces from the top and bottom magnets are termed F_t and F_b respectively. The mechanical damping coefficient is defined as c_m . The magnetic force applied by the coil is Ki . Therefore, the resulting governing equation (Eq. 15) is:

$$m\ddot{x} = c_m(\dot{b} - \dot{x}) - F_t + F_b - mg - Ki \quad (15)$$

The electrical damping is derived using the method used in the previous section. Also, the electrical damping coefficient is defined as c_e , and total damping is a summation of electrical and mechanical damping as $c_{tot} = c_m + c_e$. A change of variable, $z = x - b$, is also made to obtain a governing equation in terms of relative displacement between the magnet and casing as,

$$\ddot{z} = \frac{c_{tot}}{m}(-\dot{z}) + \frac{F_b - F_t}{m} - g - \ddot{b} \quad (16)$$

where,

$$F_t = ae^{b(L_s - z - \frac{h}{2})} + ce^{d(L_s - z - \frac{h}{2})} \quad (17)$$

$$F_b = ae^{b(z - \frac{h}{2})} + ce^{d(z - \frac{h}{2})} \quad (18)$$

Here, L_s is the length of the harvester measured from face of the bottom magnet to the face of the top magnet as shown in Figure 6a, and h is the height of the levitated magnet. The MATLAB code can be found in Appendix B.

3.4 Characterization of Magnetic Flux Density using COMSOL

The average radial flux across the coil versus the relative displacement between the magnet and the coil is required to obtain electrical damping and to calculate the voltage. A software package, COMSOL Multiphysics 3.5a, is used to approximate the magnetic flux of the middle magnet, which is used for the energy harvesting in our case. Figure 10 shows a schematic of the model developed in COMSOL.

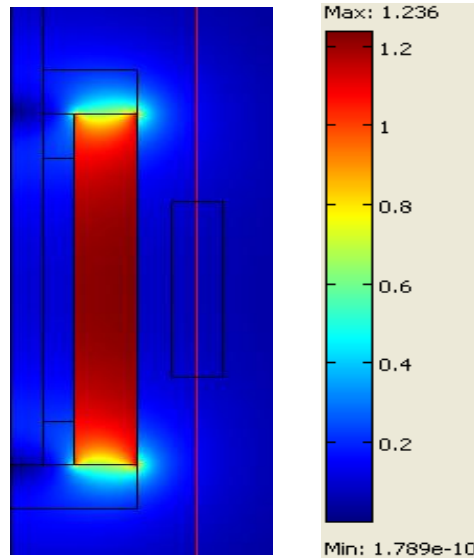


Figure 10 - Magnetic flux density of a 25.4mm (1 inch) ring magnet using a 2D axial symmetric COMSOL simulation

The coercive force or magnetization vector, M required for the simulation is determined by Eq. 19 [32],

$$B = \mu_0 H + \mu_0 M \quad (19)$$

where B , H , M , μ_0 are the magnetic flux density, magnetic field strength, coercive force and permeability of free space respectively. The remanence B_r , is the value of the magnetic flux density when the magnetic field strength is zero, and is obtained from the manufacturer's website for a N42 grade NdFeB magnet [34]. The value of B_r is 1.32T and the resulting M is 1.05×10^6 A/M. Additional information on the magnets can be found in Appendix C.

Using COMSOL simulation, the radial flux across the average diameter of the coil is obtained. The magnitude of the radial flux is dependent on distance from the magnet. The flux at the average diameter of the coil is thought to be a good representation of the average of the flux variations along its diameter.

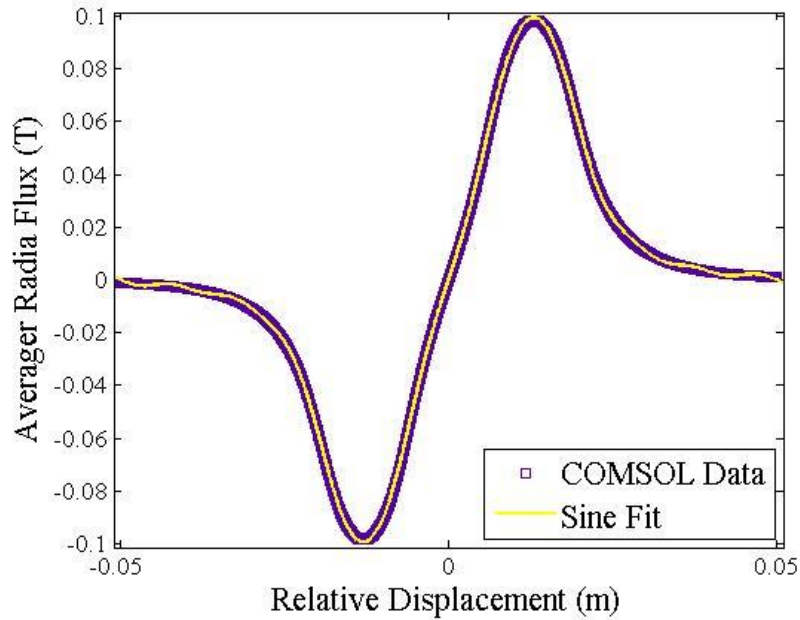


Figure 11 - Average radial flux obtained from the COMSOL simulation fitted to a sum of sine equation

Using the half height of the middle magnet and the coil as reference, the average radial flux across the height of the coil is obtained at each increment of distance between the magnet and the coil. This data set is then curve fitted using MATLAB’s curve fitting tool to formulate a function that can be used for electrical damping and voltage calculations in the model. The equation that gives the best fit has the form of sum of sine functions presented in Eq. 20.

$$B_{rad,avg}(z) = a_1 \sin(b_1 z + c_1) + \dots + a_8 \sin(b_8 z + c_8) \quad (20)$$

The coefficients obtained from the curve fit are summarized in Table 1. From Figure 11, the curve fit demonstrates a very good agreement to the simulation data.

Table 1 - Table of the coefficients for average radial flux curve fit

<i>i</i>	<i>a_i</i>	<i>b_i</i>	<i>c_i</i>
1	0.04785	62.87	9.314e-6
2	0.04399	125.6	8.007e-6
3	0.01886	188	1.0593e-6
4	0.006143	314.1	-3.142
5	0.00394	376.9	-3.142
6	0.0008607	256.3	3.141
7	0.0009059	628.3	3.142
8	0.0006762	439.8	-3.142

The numbers in the first column denotes the subscript to the parameters a , b and c .

Chapter 4: Experimental Setup

Measurement devices are used to determine the energy harvester's response to the excitation. The equipment used in the experiment and their setup with is described in detailed. In addition, the fabrication of the prototypes is outlined. Lastly, experiments are performed to characterize the magnetic force and the mechanical damping of the prototypes.

The experimental setup consists of the prototype energy harvester mounted onto a test structure as shown in Figure 12. The test structure is subjected to constant amplitude of input excitation acceleration over a defined range of frequencies.

4.1 Test Equipment and Sensors

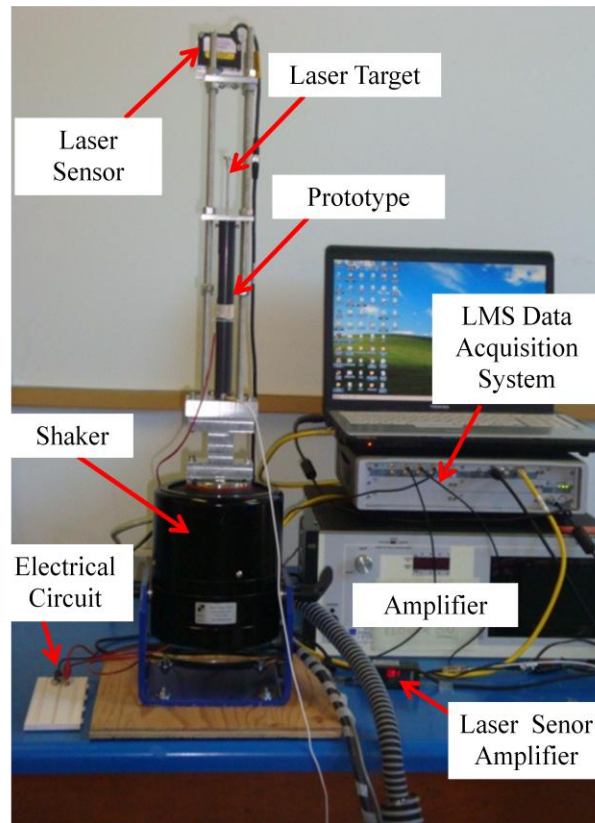


Figure 12 - Experimental setup

The test structure is used to secure the energy harvester unit in place and to provide mounting for the sensors. The setup, as depicted in Figure 12, consists of a signal generator, an amplifier, a shaker, a laser displacement sensor, an accelerometer, test structure, the prototype, a load circuit, and a data recorder. The testing process is as follows: the signal generator provides a control

signal through the amplifier to the shaker to excite the energy harvester unit. The signal is then controlled by an accelerometer mounted on the structure using a close feedback loop. The energy harvester unit generates an EMF and powers a load circuit. The signal is a sinusoidal wave with constant acceleration amplitude, swept through a defined frequency range. A laser displacement sensor mounted on the top of the structure measures the energy harvester's middle magnet's displacement response. The voltage across the load resistor is recorded.

4.1.1 Excitation Mechanism

A shaker is used as the excitation mechanism for the test structure. The selected shaker is a Model Shop 2075E Electroynamics shaker. The maximum output force supplied by the shaker is 334N with a frequency range up to 6500 Hz and it has a stroke of 1 inch. Appendix D outlines a complete data sheet for the shaker. A sinusoidal acceleration excitation with constant amplitude of 0.35g and 0.5g is applied to the test structure and energy harvester unit. The lower range of its operating frequency is limited by the level of the applied acceleration and the stroke. For example, for 0.5g, the lowest operational frequency of the shaker is 3.13Hz as determined by Eq. 12. To keep base acceleration constant at lower frequencies, the stroke must be increased.

The test structure is attached to a spacer to separate the prototype from the shaker and to avoid any influence of the magnetic field of the electroynamics shaker on the permanent magnets in the prototype.

4.1.2 Signal Generation, Sensing Mechanisms and Data Recorder

Both signal generation and data recording are handled using an LMS SCADA MOBILE V data acquisition system (DAS) with a V8 voltage and ICP input module, and a XSI-V control module for close loop control of the sine waveform. A CAT 5 Ethernet interface allows LMS DAS to operate with its LMS Test Lab software running on a Toshiba laptop. As a result, signal generation and data recording is implemented using Sine control module of the Test Lab software. A schematic of the LMS DAS system architecture is depicted in Figure 13.

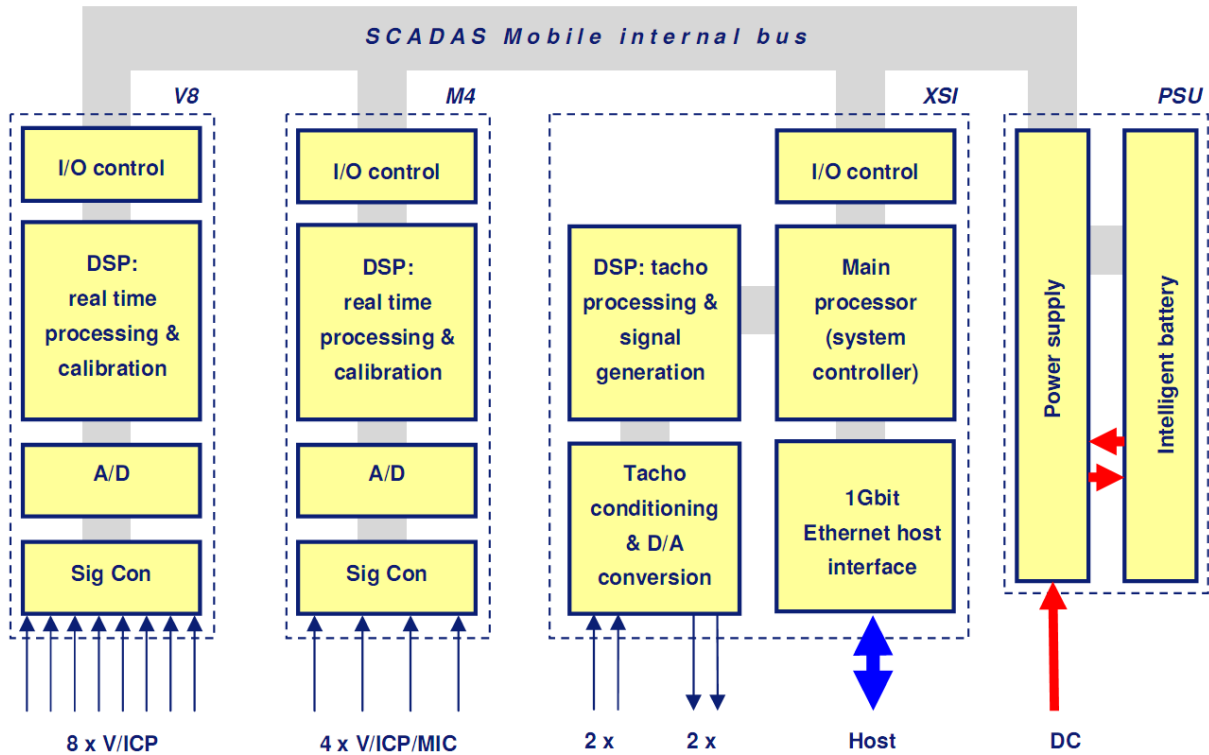


Figure 13 - Schematic diagram of the SCADAS Mobile internal architecture [35]

An accelerometer mounted at the bottom of the test structure is used to measure the acceleration of the test structure and control the input signal using a feedback loop. The accelerometer, manufactured by Dytran (model 3035AG), measures the acceleration in a single axial direction. The selected accelerometer has a frequency range between 0.5 Hz and 10,000 Hz with a sensitivity of approximately 100mV/g. Please refer to Appendix D for the complete datasheet on the accelerometer used in this experiment. The accelerometer outputs a voltage signal which is fed into an analog input port on the V8 module in the LMS DAS. Sine Control is calibrated to output acceleration level. Note that the accelerometer is calibrated based on its factory calibrated settings.

A laser displacement sensor is used to measure the displacement of the middle magnet of the prototype harvester. The laser sensor is mounted at the top of the test structure. The laser sensor measures the displacement of a target that protrudes from the energy harvester, but is also firmly attached to the middle magnet of the energy harvester. The selected laser displacement sensor is an analog laser sensor manufactured by Keyence, model IL-100. The laser sensor has a displacement measuring range of 55mm in a single axial direction. The output measurement is analog voltage or amperage. The laser displacement sensor is able to take reading at a speed up

to 5000Hz. Refer to Appendix D for the complete datasheet. Analog voltage signal is fed into the analog input port located on the V8 module of LMS DAS. Sine Control is calibrated based on the output setting selected on the displacement sensor. For this experiment, 0-5V output range is selected, which correspond to a sensitivity of 125mV/mm.

A load circuit is formed by connecting the two ends of the coil on the energy harvester to a bread board. A load resistor is connected in series with the coil on a bread board. Load voltage is measured by creating a parallel loop across the load resistor using alligator clips and the reading is directly fed into the analog port on the V8 module of the LMS DAS. Sine Control is calibrated to read the voltage directly, at one to one ratio.

4.2 Prototype Design

The prototype energy harvesters are show in Figure 14. Both the MDOF and SDOF harvester consists of three major components: the exterior casing, the middle magnet assembly, and two end magnet assemblies. Refer to Appendix E for additional images. The exterior casing includes the enclosure of the energy harvester as well as the conducting coil. The middle magnet assembly includes a permanent magnet and the laser target probe. The end magnet assembly for the SDOF harvester includes a permanent magnet and an end attachment. The end magnet assembly for the MDOF harvester is similar to the SDOF end magnet assembly but also includes a compression spring. The prototypes are fabricated mainly from non-magnetic materials such as aluminum and PVC plastic. Some of the bolts are made from stainless steel due to the lack of availability of fasteners made from non-magnetic materials. The permanent magnets are purchased from KJ Magnetics. They are axially magnetized N42 grade NdFeB ring magnets. Refer to Appendix C for more details. Detailed discussion of all major components and final assembly are provided in the subsequent sections.



Figure 14 – Prototype energy harvesters: SDOF (left) and MDOF (right)

4.2.1 Exterior Casing

The exterior casing is made from a 0.5 inch schedule 80 PVC pipe with an inner diameter of 0.524in. The pipe is milled to the required length to form the casing. The difference between the SDOF and the MDOF casing is the length. A 0.5 inch by 0.1 inch slot is made at the middle of the casing for the copper coil winding. The coil height is limited to 0.5 inch to avoid interference from the top and bottom magnets. A 4000 turn coil is wound by SG. Smallwood, a company located in Kitchener, Ontario, Canada, using 40 AWG copper wires. Two 4-40 bolt holes are fabricated at each end of the casing for bolts to secure the end magnet assembly to the casing.

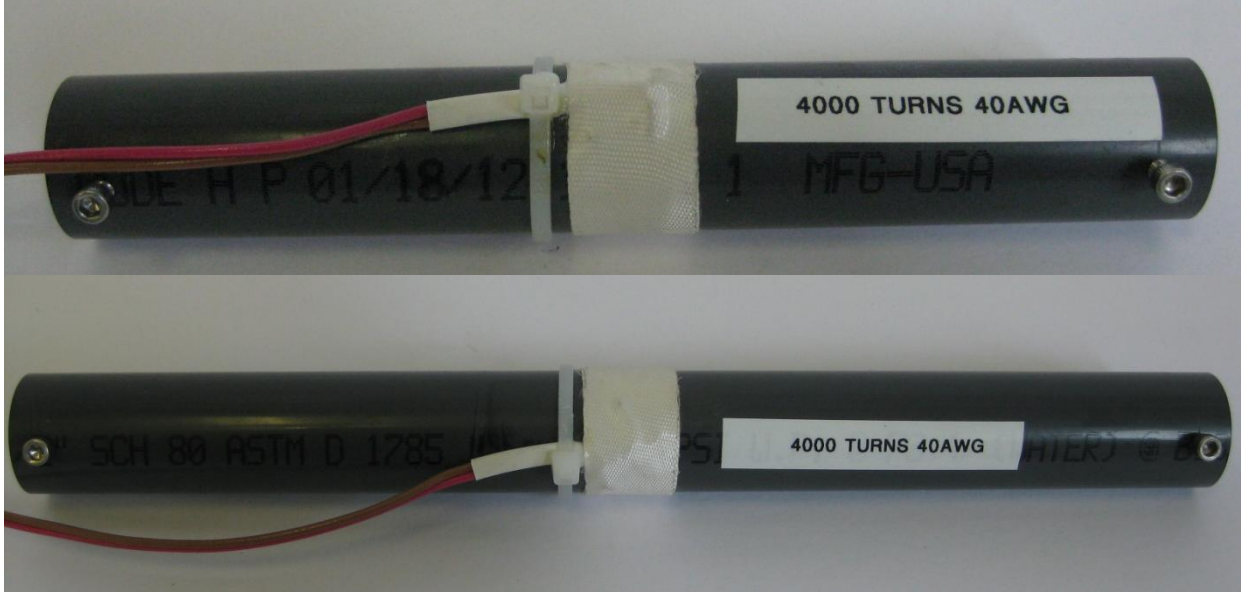


Figure 15 –Exterior casings: SDOF (top) and MDOF (bottom)

4.2.2 Middle Magnet Assembly

The middle magnet assembly is the same for both the SDOF and MDOF harvesters. The magnet used in the middle magnet assembly is 1 inch in length with a 0.5 inch outer diameter and a 0.25 inch inner diameter. Two disks fabricated from 0.5 inch diameter aluminum rod are glued to each end of the permanent magnet using epoxy. The disks allow a 0.125 inch diameter aluminum rod to be inserted through the center of the magnet and protrude out of the energy harvester. Another disk sits on top of the protruding rod, where it acts as a target for the laser displacement sensor.



Figure 16 - Middle magnet assemblies: SDOF (top) and MDOF (bottom)

4.2.3 End Magnet Assembly

The magnet in the end magnet assembly is 0.5 inch in length with a 0.5 inch outer diameter and a 0.25 inch inner diameter. For the SDOF system, the magnet is glued with epoxy to an end attachment fabricated using 0.5 inch diameter aluminum rod. For the MDOF system the magnet is glued with epoxy to a spacer, which is glued to the spring and the spring is also glued to the end attachment. The spacer is also fabricated from 0.5 inch diameter aluminum rod. The spring selected is a stainless steel compression spring with a stiffness of 35N/m, manufactured by Lee Spring Company.



Figure 17 – End magnet assemblies: SDOF (left) and MDOF (right)

4.2.4 Final Assembly

There are four major steps to the final assembly:

1. An end magnet assembly is inserted into the casing and secured with two stainless steel bolts, making sure it is flush with the end of the casing
2. The middle magnet assembly is lowered into the casing with the correct orientation for magnetic repulsion
3. The other end magnet assembly is inserted into the open end of the casing. It is secured using two stainless steel bolts to ensure it is flush with the end of the casing
4. The laser target disk is placed atop of the protruding rod of the middle magnet assembly

The middle magnet assembly is the same design for both the SDOF and MDOF prototype. The protruding rod can be changed as necessary to provide sufficient length of travel for the experiment. The same middle magnet assembly is used on both prototypes.

4.3 Test Structure

The test structure is fabricated entirely using aluminum to avoid interference with the permanent magnets. It consists of 1/2 inch base plate, four 1/4-20 threaded rods, a 1/2 inch top plate and a laser

sensor mount. Its purpose is to secure the prototype firmly to the shaker table and provide a mounting location for the laser sensor. Since the laser sensor is fixed with respect to the test structure and prototype, and in turn, the shaker table, the measure displacement of the moving mass of the prototype would be relative displacement with respect to the base.

The base plate of the test structure provides a bolt clearance hole on each end, allowing for mounting to the spacer and in turn, the surface of the shaker table. It also has four threaded holes for the threaded rods, which supports the entire structure. The test structure is designed with two methods of securing the test piece. The first method is using the top and base plate to clamp and secure the prototype to the test structure. The second method uses a ½-20 bolt through the center of the base plate to attach to a threaded hole at the bottom of the prototype. The top plate has a ¼ inch hole at the center for the rod of middle magnet assembly to pass through.

Two ¼ inch plates are jointed to form the laser sensor mount. The laser sensor is mounted to the vertical plate. There is a slot on the horizontal plate to allow for the adjustment of the laser sensor in one planar axis. The horizontal plate sits on top of 4 nuts threaded onto the threaded rods and its vertical position can be adjusted through changing the position of the nuts. The mount is secured to the rest of the test structure by tightening nuts against the horizontal plate.

4.4 Experimental Procedure

The experiment is performed by an application of a sinusoidal sweep through a defined frequency range. The sinusoidal sweep is performed by increasing the frequency, low to high, as well as decreasing the frequency from, high to low, known as forward sweep and backward sweep respectively. The reason that both forward and backward sweeps are performed is to determine if the system has undergone bifurcation, which is one of the characteristics of a non-linear system. For each sweep, the peak, RMS and harmonic value of each variable (base acceleration, relative displacement and voltage) are recorded. The key component to this experiment is determining sinusoidal sweep parameters: the frequency range, the excitation level, the sweep rate, and the control method.

First, the frequency range and excitation level are determined. Sinusoidal sweep is performed on the prototypes using different excitation levels from 4 Hz to 20 Hz. The results of the experiment are analyzed. It is determined that frequency range is more than adequate to show

the key characteristic of the frequency response curve since the main peaks for the SDOF and MDOF prototypes are at approximately 4 Hz and 7 Hz respectively. Thus, the frequency range is narrowed to the range of 4 Hz to 16 Hz for experiment run time efficiency.

As for the excitation level, at 0.65g, loud noises were heard from the MDOF prototype at frequencies around peak displacement. This was because the bottom magnet was making contact with the end of the tube. Thus, the maximum excitation level is limited to 0.6g. Two excitation levels are chosen from the range of 0 to 0.6g that provides sufficient excitation to induce a sufficient response in the system and they are 0.35g and 0.5g.

Next, the sweep rate and control method are determined. The sinusoidal sweep performed is a continuous sweep. The software does not have a feature to dwell, which is ideal to ensure a steady state response at each frequency. Thus, a very slow sweep rate of 0.01Hz/sec is first conducted. The sweep rate is increased and the new results are compared to the previous results of the slower sweep rate. The optimal sweep rate is determined to be 0.05Hz/sec, a rate which reduce experiment run time without altering the results.

Sine Control has four amplitude estimate methods used for controlling the sine waveform; harmonic, RMS, average, and peak. At each frequency resolution, values are calculated from the data block obtained in that frequency resolution using the estimate method. Each of these estimate methods, the maximum, minimum or average value can be used. The harmonic control method is default, and the best method in the opinion of the technical staff at LMS Support. The harmonic method offers the best estimate for the fundamental frequency and provides excellent harmonic rejection [36]. However, all control methods are performed and the results compared. The control method does not have a significant effect on the result. Regardless, at low frequency, the controller has difficulty keeping the acceleration level at the target value. This issue will be discussed further in the experimental results section in Chapter 5. The maximum value is used because a constant peak base acceleration is desired.

The final parameters for the experimental are outlined in Table 2.

Table 2 – Table of the sine sweep parameters

Parameter	Value
Frequency Range	4 – 16 Hz
Base Acceleration	0.35g, 0.5g
Sweep Rate	0.05Hz/sec
Control Method	Harmonic: Maximum

4.5 Characterization of Magnetic Force

4.5.1 Test Setup

The test setup for obtaining the magnetic force versus the separation distance consists of a 10lbf Chatillon force gauge, and a Keyence IL-100 laser sensor shown in Figure 18. The Chatillon force gauge measures tension or compression force in a single direction. The measurement is displayed at 0.05N increments. Please refer to Appendix D for the complete datasheet. The cylindrical tube containing two magnets under repulsive forces is placed directly below the force gauge. This tube is held in place by a plastic tab using scotch tape. The force gauge is used to push down the top magnet and to measure the force between the magnets. The laser sensor is attached to the arm of the test stand where it is fixed to the force gauge. The sensor reflects on a fix target on the test stand and measures at 0.01mm increments. The data is displayed on an LED display on the amplifier of the laser sensor.

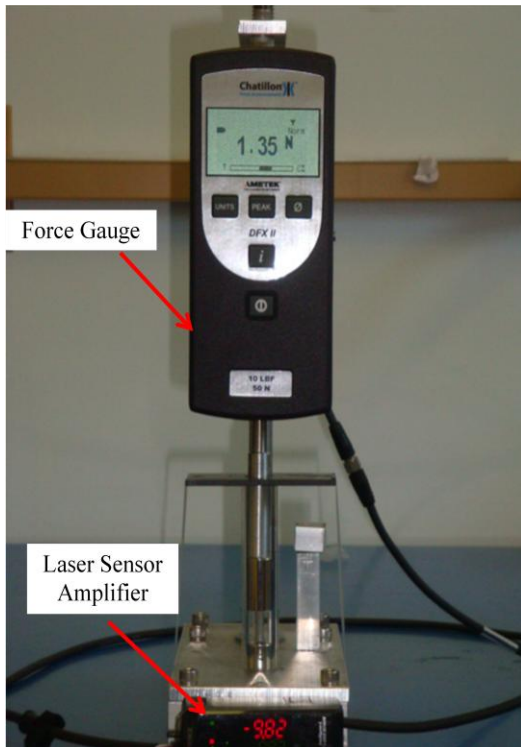
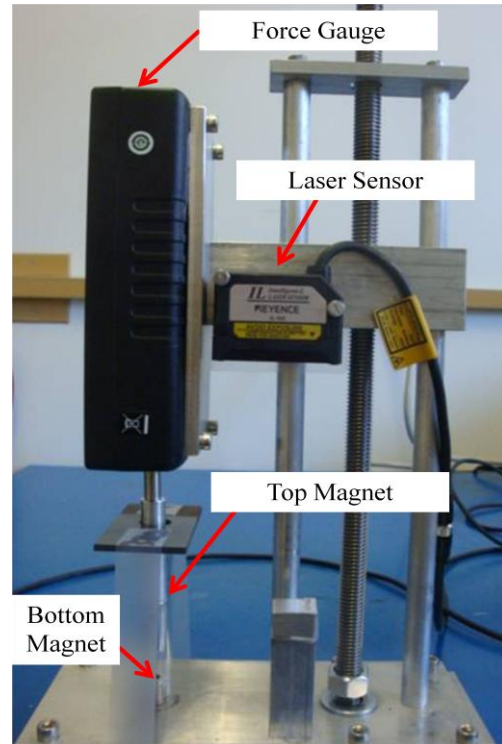


Figure 18 – Magnetic force characterization test setup



4.5.2 Test Procedure

The characterization is performed using the following procedures:

1. The mass of the levitated magnet is measured using a scale and a non-magnetic spacer to avoid interference between the magnet and the stainless steel plate of the scale
2. The bottom magnet is placed on the test stand directly under the force gauge, for smaller magnets, it might be necessary to secure it in place with tape
3. The cylindrical tube is placed on the test stand over the magnet
4. The second magnet is placed inside the cylindrical tube, levitated under repulsion force
5. The cylindrical tube is positioned directly under the force gauge and secured in place
6. The force gauge and laser sensor are powered and checked to ensure correct readings
7. The force gauge is lowered into the tube until contact is made between the two magnets and zero separation distance is established.
8. The force gauge is raised 1mm and the force reading is taken
9. Step 6 is repeated until separation occurs between the levitated magnet and the force gauge

- The force gauge is lowered into the tube, and measurement are taken at the same separation distance to ensure repeatability

4.5.3 Curve Fitting

The curve fitting tool in MATLAB is used to find an analytical equation in the form of an exponential function that would best characterize the data points obtained in testing. A curve fit using an exponential equation, $F(s) = ae^{bs}$, was performed, but proved inadequate for a good fit. A more complex form of the exponential equation (Eq. 21) is used.

$$F(s) = ae^{bs} + ce^{ds} \quad (21)$$

Where F , and s are the repulsion force in Newton, and separation distance in meter respectively. Also a , b , c , and d are constant coefficients, determined through curve fitting using a least square procedure.

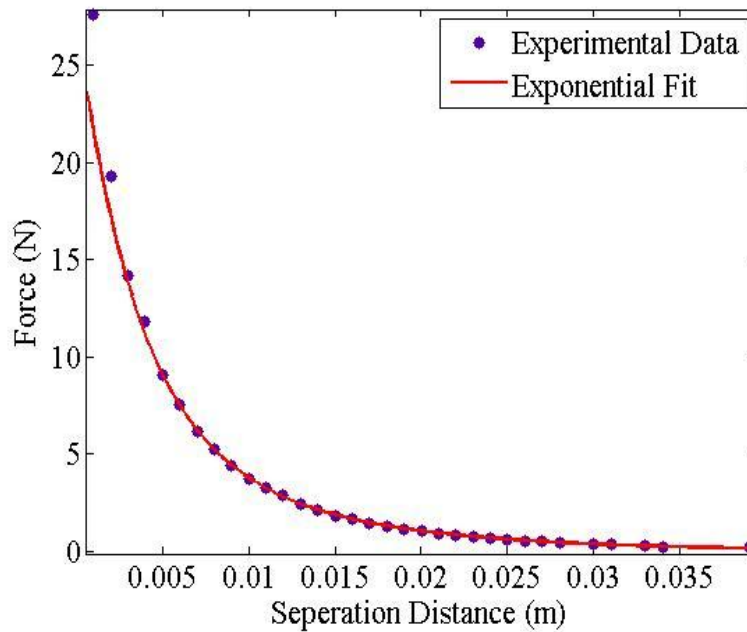


Figure 19 – Magnetic repulsion force data plotted with the curve fit

As shown in Figure 19, Eq. 21 is able to provide a much better curve fit and the fitted exponential curve shows good agreement with the experimental data. To improve the curve fit, the first 5 data points where separation distance is 1mm to 5mm are ignored. These data points are the least repeatable in the characterization test and are irrelevant because the magnets are

unlikely to come so close to each other inside an energy harvester. The coefficient found are $a=20.38$, $b=-288.9$, $c=7.049$ and $d=-98.55$.

4.6 Damping Characterization using Log Decrement Method

Logarithmic decrement method is used to find the damping ratio of an underdamped structure by observing the logarithmic decay of the structure in time domain initially perturbed [37]. This method assumes the system is linear, which is acceptable in this case when the displacement amplitudes are small. From the damping ratio, the damping coefficient of a system can then be calculated. Using this method, the mass-spring-damper system is displaced from its equilibrium position. The displacement versus time is recorded and the damping ratio as well as other parameters is extracted based on Eq. 22 [37]. This method is employed to find the mechanical damping coefficient for each degree of freedom of the prototypes.

$$x(t) = Ae^{-\zeta\omega_n t} \sin(\omega_d t + \phi) \quad (22)$$

Where x , A , ζ , ω_n , ω_d , ϕ are the displacement, amplitude, damping ratio, undamped natural frequency, damped natural frequency, and the phase shift respectively.

4.6.1 Damping Measurement Test Setup

The equipment used in this experiment includes the test structure, a Keyence IL-100 laser displacement sensor, and the LMS data acquisition unit. The Spectra Testing module of the LMS Test Lab software was used for this test. The laser sensor is set to record data at 5000Hz, its maximum sampling rate. The analog output is set to output 0 to 5 Volts corresponding to -20mm and +20mm respectively. Spectra Testing is calibrated using this information resulting in a sensitivity of 0.125V/mm. Refer to Appendix D for full datasheet. The laser sensor is mounted on top of the test structure. The structure is excited, and the displacement versus time data is captured by the LMS DAS. Spectra Testing is set to record for 5 seconds.

The damping test is performed for the middle magnet of both the SDOF and MDOF prototype. Tests are also performed on the end magnet assembly of the MDOF prototype. For the middle magnet of the SDOF and MDOF harvesters, the respective prototypes are assembled using an exterior casing fabricated without a coil winding. The middle magnet is initially perturbed by pushing the laser target downward and let it vibrate freely. The laser sensor measures the

displacement in time domain. For the testing of the end magnet assembly, one of the end magnet assemblies is put into a shorter exterior casing. The ¼-20 bolt is used to secure this test piece to the test structure, by threading it to the bottom of the end magnet assembly. The laser sensor reflects off the top surface of the magnet. A metal screw driver is used to attract the magnet and lift it to initially perturb the system.

4.6.2 Test Procedure

The test procedure is as follow:

1. The test prototype is assembled
2. The prototype is placed on the test structure and secured in place
3. The vertical position of the laser sensor mount on the test structure is adjusted until the equilibrium position of the test prototype is approximately 0 mm.
4. LMS Test Lab Spectra Testing data recording starts measuring
5. The prototype is perturbed
6. Data is recorded and saved

4.6.3 Curve Fitting

The test data are presented in Figure 20 for middle magnet of SDOF harvester, Figure 21 for middle magnet of MDOF harvester, and Figure 22 for the end magnet of the MDOF harvester. The curve fitting tool in MATLAB is used to find the coefficients in Eq. 23 using a least square procedure.

$$x(t) = ae^{-bt} \sin(ct + d) \quad (23)$$

Where

$a = A$, $b = \zeta\omega_n$, $c = \omega_d$, and $d = \phi$.

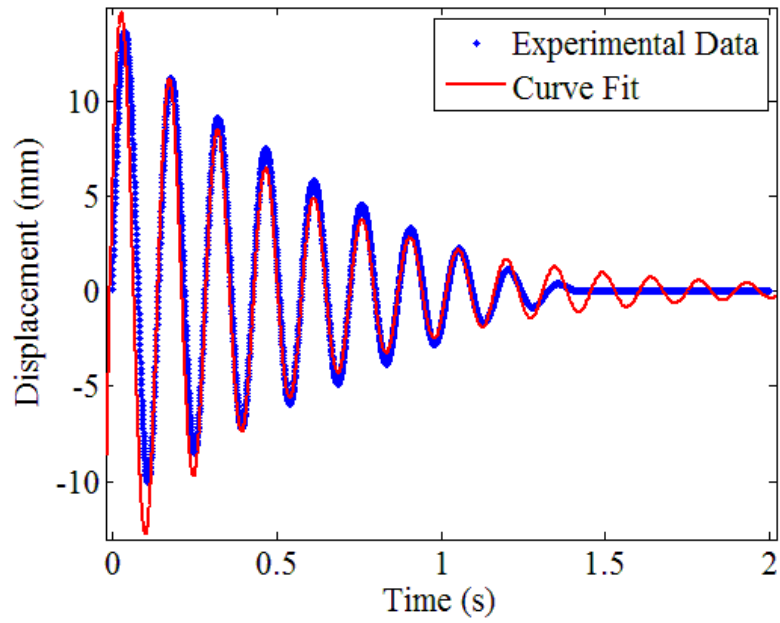


Figure 20 – SDOF: middle magnet damping data with the curve fit

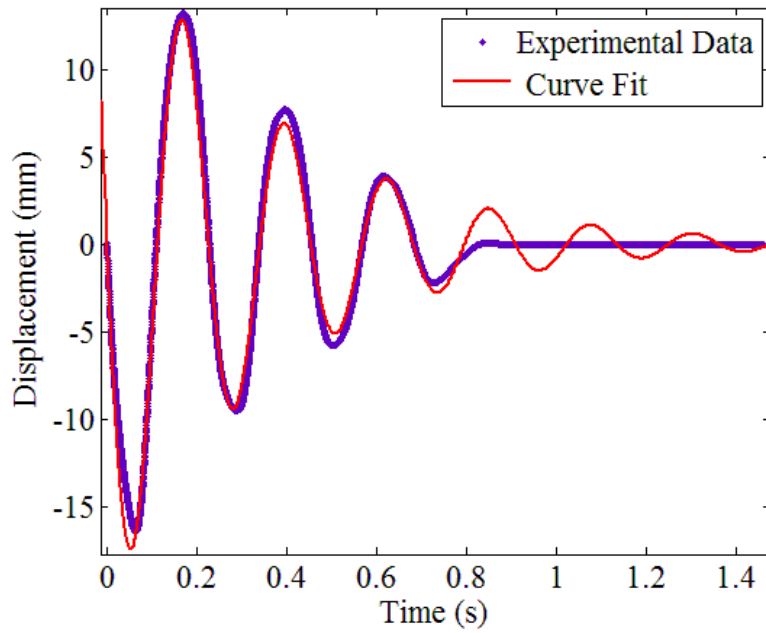


Figure 21 – MDOF: middle magnet damping data with the curve fit

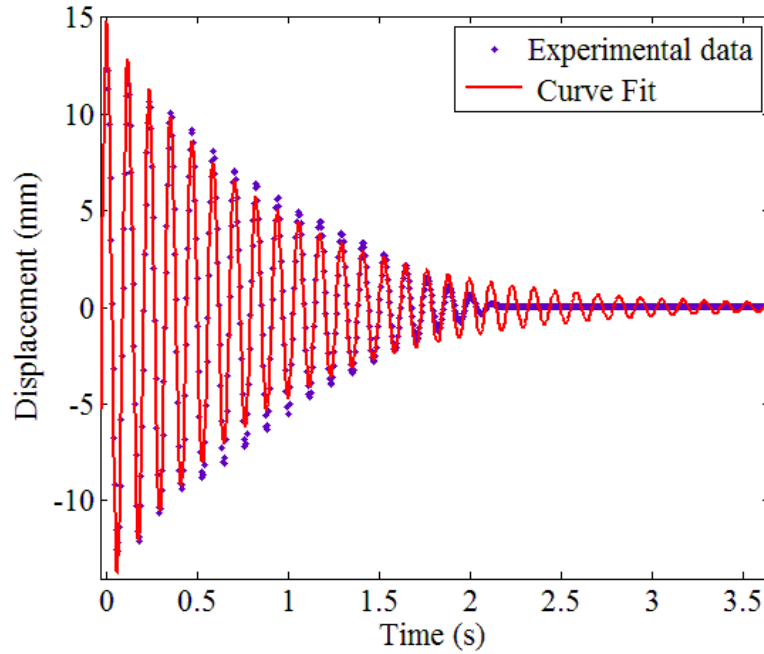


Figure 22 – MDOF: end magnet damping data with the curve fit

These figures show that the curve fit is in good agreement with the experimental data. An interesting point is that there is some variation in the periods of oscillations in Figure 20 and Figure 21. This is expected due to the nonlinearity. Due to the nonlinearity, the stiffness is dependent on the amplitude of the displacement. As the displacement decreases, the stiffness is lowered, thus resulting in a slight change in the period of oscillation. In addition, the discrepancies at large time periods are due to the effect of friction, which is not accounted for in this method.

The key coefficient required is $b = \zeta\omega_n$ in Eq. 23 which is equivalent to the summation of damping ratio and natural frequency. Using Eq. 24, the mechanical damping coefficient can be obtained from the coefficient b , where m is the suspended mass. The results are summarized in Table 3.

$$c_m = 2\zeta\omega_n m = 2bm \quad (24)$$

where c_m is the mechanical damping coefficient.

Table 3 – Table of the damping test data

Parameter	Middle Magnet SDOF	Middle Magnet MDOF	End Magnets MDOF	Unit
<i>b</i>	1.86	2.703	1.148	-
<i>m</i>	0.0257	0.0267	0.0125	kg
<i>c_m</i>	0.0956	0.144	0.0287	N s/m

Chapter 5: Experimental Validation of the Developed Model

In this chapter, frequency response functions are generated by the model developed in Chapter 3 using the experimental parameters obtained previously. The model results are then compared with the experimental data to give support to the validity of the model. Lastly, the model's ability to predict bifurcation is briefly examined.

Table 4 summarizes the system parameters obtained in experiments. The damping value is obtained using log decrement method outlined in the previous chapter. The lengths of the harvesters are measured using a caliper.

Table 4 – Parameter values measured for SDOF and MDOF harvesters

Parameters	SDOF	MDOF	Units
m_1	-	0.0125	kg
m/m_2	0.0257	0.0267	kg
m_3	-	0.0125	kg
k_1	-	35	N/m
k_3	-	35	N/m
c_{1m}	-	0.00287	-
c_m/c_{2m}	0.0956	0.144	-
c_{3m}	-	0.00287	-
LS_1	-	0.0254	m
LS_3	-	0.0254	m
h_1	-	0.0127	m
h/h_2	0.0254	0.0254	m
h_3	-	0.0127	m
L_s/L_m	0.098	0.2037	m
l_{coil}	236.2	236.2	m
R_{load}	1000	1000	Ω
R_{coil}	845	845	Ω

5.1 Numerical Results

The governing equations of motions in Chapter 3 are solved numerically using ODE45 functions in MATLAB. The complete code for the model can be found in Appendices A and B. The electrical damping shown in Eq. 8 is integrated in the model, and the damping value is updated at each numerical step. The model determines the frequency response functions of the system (SDOF and MDOF devices) from 4 to 16 Hz with a frequency increment step of 0.1Hz. At each increment, the model finds the relative displacement, and the voltage across the external load in

time domain to ensure the response reached the steady state condition. For each of these variables, the upper and lower peak values are determined from the data in the last 10 seconds of the simulation. The average values for each variable is then found. This process is repeated for each frequency step, and the results are plotted with respect to frequency to find the frequency response function of the system. The initial displacements for the first frequency step are based on the geometric parameters of the system and the initial velocities are zero. Constant base acceleration amplitudes of 0.35g and 0.5 are applied to both the SDOF and MDOF devices, similar to the experiment. Forward and backward sweeps are performed to check for bifurcation. No evidences of bifurcation is found. The resulting frequency response functions for middle magnet of SDOF harvester magnet can be seen in Figure 23 to Figure 24. The response function of the top, middle and bottom magnets of the MDOF harvester can be seen in Figure 25 to Figure 27 for system parameters in Table 4.

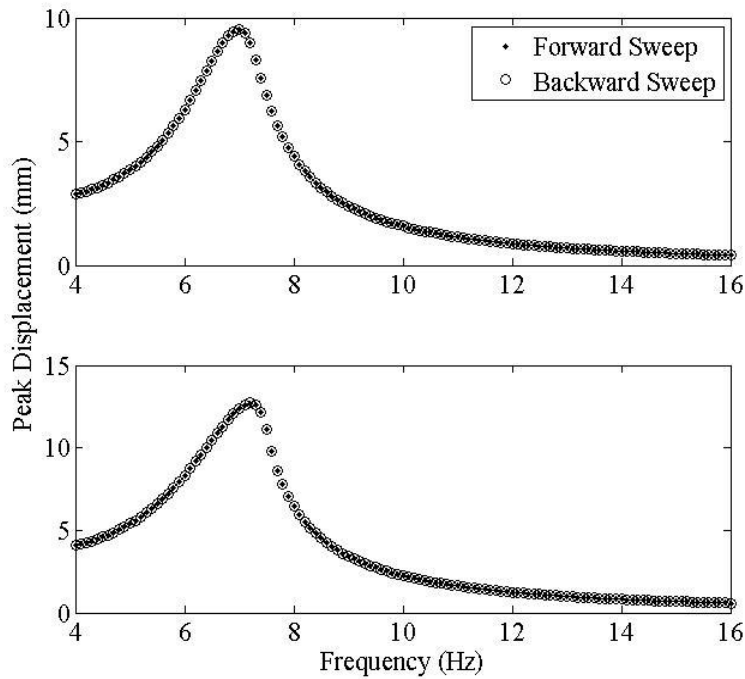


Figure 23 – Peak displacement vs. frequency graph by the model for the SDOF harvester at 0.35g (top) and 0.5g (bottom)

The peak voltage is also plotted in Figure 24. The peak response occurs at approximately 7Hz with peak displacement of 9.5mm and 12.7mm for each of the accelerations levels respectively. The peak voltage is 4.3V and 6.3V for 0.35g and 0.5g base accelerations respectively. Model predictions for SDOF are in good agreement with Mann and Sims’ results where nonlinearity is

not engaged [22]. The frequency response function predicted by the model shows it is operating in the linear region. Forward and backward sweeps show one single stable solution for all frequencies and thus there is no evidence bifurcation has occurred. Nonlinear response is highly dependent on the damping and base acceleration. The combined mechanical and electrical damping for this system is fairly high. Therefore, the relatively low base acceleration levels are insufficient overcome the high damping in the system to engage bifurcation. However, at 0.5g base acceleration, the frequency response curve has a slight lean towards the right, which is an indication of non-linearity. This is the beginning of the ‘backbone’ curve, a characteristic of spring hardening systems [18, 38].

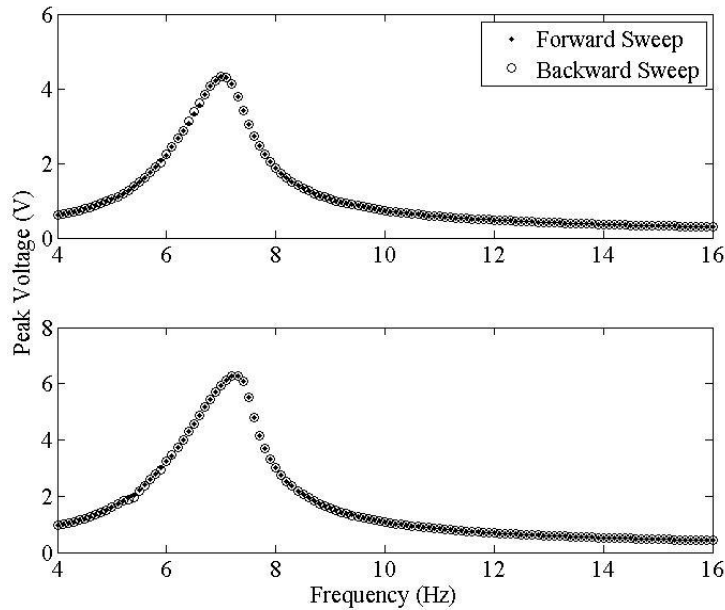


Figure 24 - Peak voltage vs. frequency graph by the model for the SDOF harvester at 0.35g (top) and 0.5g (bottom)

The peak relative displacement vs. frequency graph for the top, middle and bottom magnet in the MDOF harvester are shown in Figure 25 for 0.35g and in Figure 26 for 0.5g base acceleration respectively. Also, the peak voltage vs. frequency graphs for the middle magnet is shown in Figure 27. The peak response of the middle magnet is approximately at 4.2Hz with a peak relative displacement of 16.1mm and a peak voltage of 5.3V at 0.35g and 25.1mm and 8.85V at 0.5g. The predicted frequency response functions also show three smaller peaks at approximately 5Hz, 9.3Hz and 12.5Hz, a characteristic of a MDOF system. Compared to SDOF

harvester, the frequency of main peak is at a lower frequency. In addition, the displacement and the load voltage are much higher compared to the SDOF system at the same base excitation level, an improvement in design. Therefore, the MDOF harvester is capable of producing more electrical power. Furthermore, the top and bottom magnets are not used for energy harvesting in the prototype, but they can be used to generate more power.

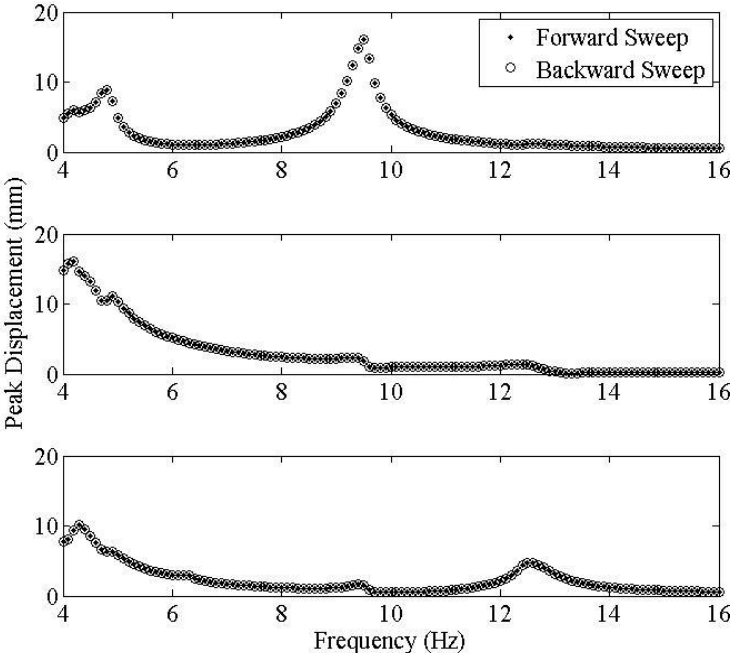


Figure 25 -Peak displacement vs. frequency graph by the model for the top, middle, and bottom magnets of the MDOF harvester at 0.35g

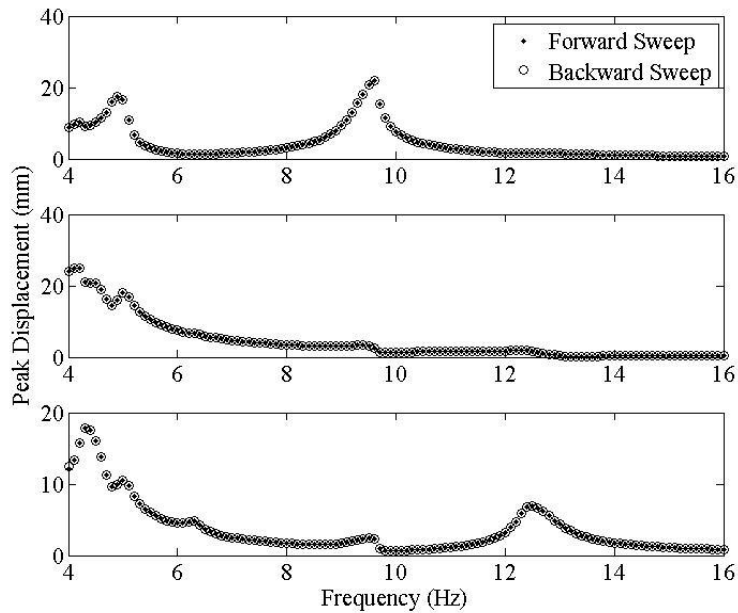


Figure 26 - Peak displacement vs. frequency graph by the model for the top, middle, and bottom magnets of the MODF harvester at 0.5g

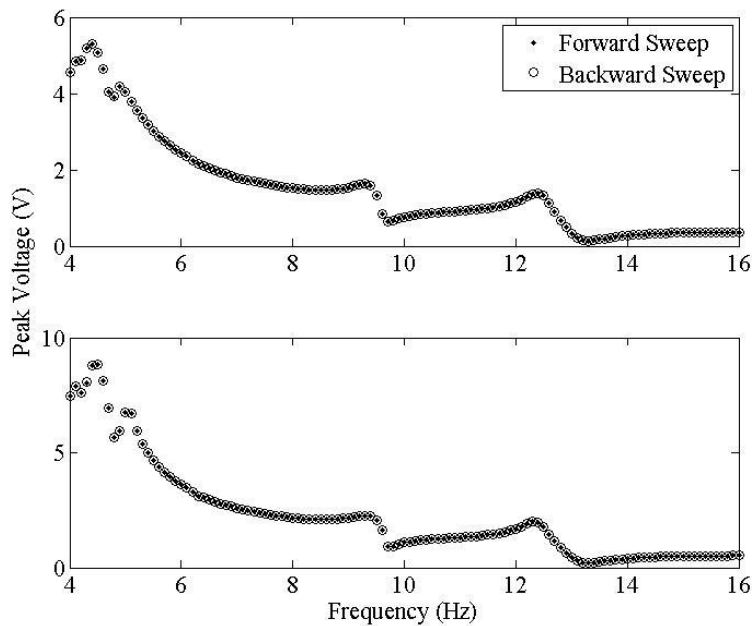


Figure 27 - Peak voltage vs. frequency graph by the model for the middle magnet of the MODF harvester at 0.35g (top) and 0.5g (bottom)

The predicted frequency response function for the top magnet shows two peaks at approximately 4.8Hz and 9.5Hz. These peaks coincide with the peaks in the frequency response function of the

middle magnet. For the bottom magnets, four peaks at approximately 4.3Hz, 5Hz, 9.4Hz and 12.4Hz coincides with the peaks of the frequency response function for the middle magnet. In addition, the spring stiffness of the top and bottom magnet can be changed independently to achieve peak responses at the desired frequencies.

For the forward and backward sweeps, the model prediction of frequency the response curve did not show multiple solutions for any of the magnets. Similar to the case of the SDOF, the damping in the MDOF system is high enough to avoid bifurcation.

5.2 Model Validation

Experimental frequency response functions are obtained using the procedure and parameters outlined in Chapter 4. The experimental data is compared with the model predictions to validate the model. The SDOF results are shown in Figure 28 and Figure 29. Also, the MDOF harvester data and comparison are shown in Figure 31 and Figure 32.

The model predictions for SDOF harvesters agree well with the experimental results. Small discrepancies are evident in the voltage results at low frequencies. The main reason is that the peak acceleration at low frequencies is higher than the desired target value. The peak base acceleration at lower frequencies at times, seen in Figure 30, can be as much as 50% higher than the desire value of 0.5g. The equipment in the experiment setup is not able to adequately control the peak acceleration at low frequencies and this issue is not resolved. The peak voltage predicted by the model is lower than the experimentally data around the peak response frequencies. One plausible explanation is the underestimation of the radial flux by the simulation or the actual flux is higher than the manufacturer's specification. Due to the length of the coil in the prototype and the relatively high relative velocity at peak response, a small change in average radial flux will produce a large change in the peak load voltage.

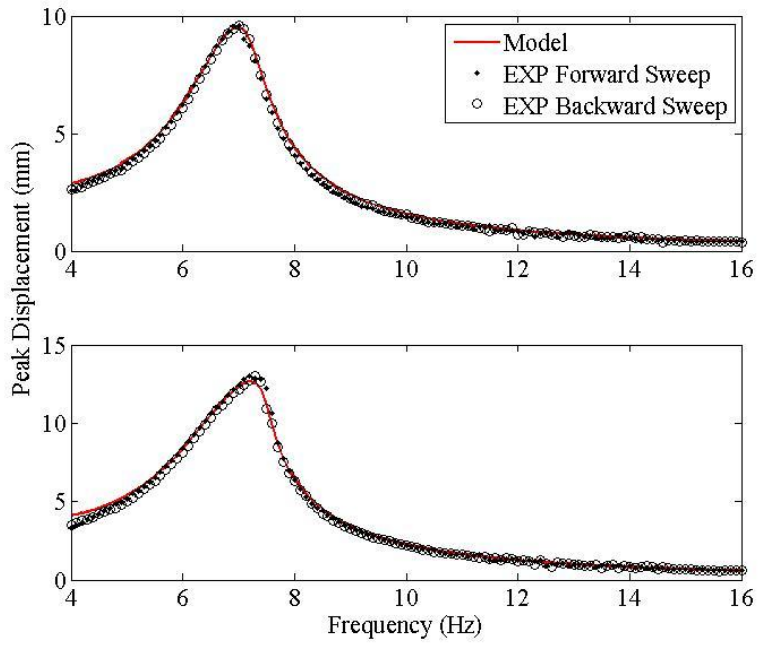


Figure 28 - Peak displacement comparison between the experimental results and the model for the SDOF harvester at 0.35g (top) and 0.5g (bottom)

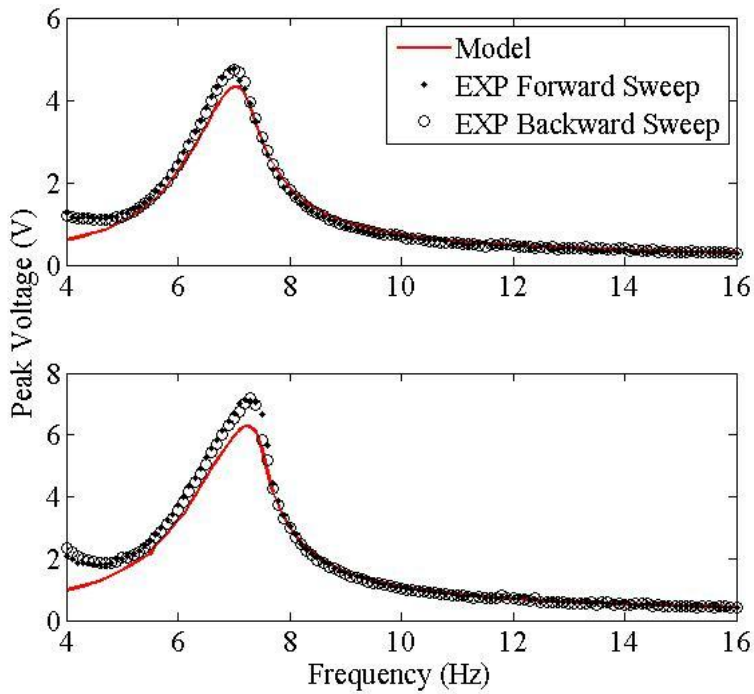


Figure 29 - Peak voltage comparison between the experimental results and the model for the SDOF harvester at 0.35g (top) and 0.5g (bottom)

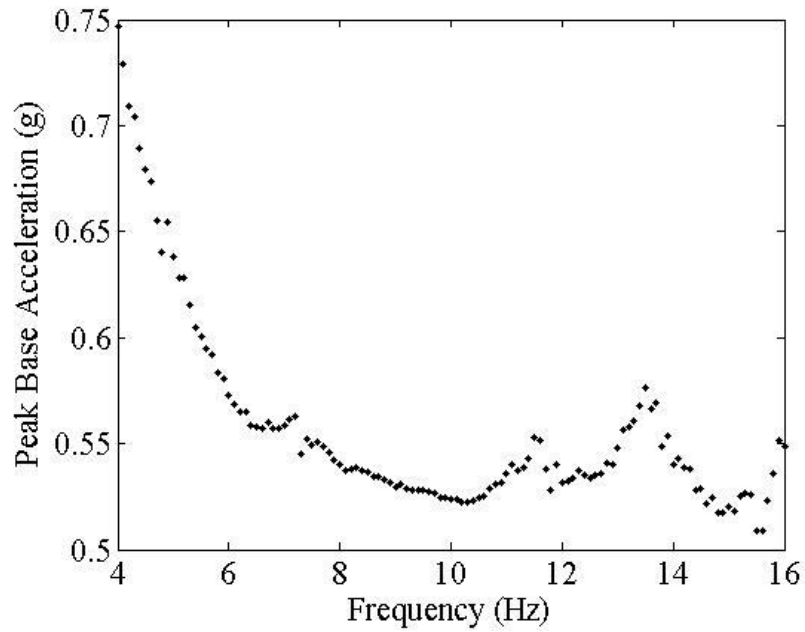


Figure 30 – Sample base excitation acceleration data recorded by the accelerometer with a target value of 0.5g.

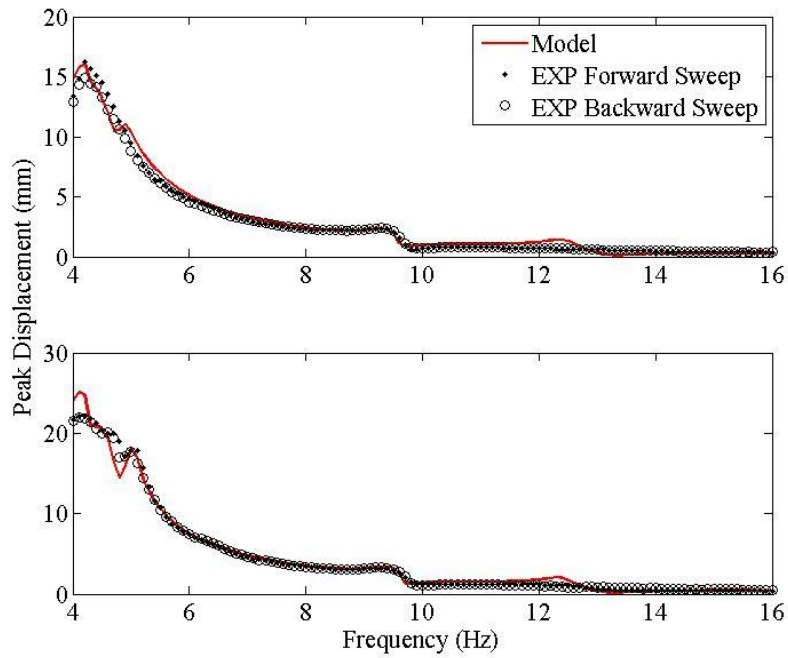


Figure 31 - Peak displacement comparison between the experimental results and the model for the middle magnet of the MDOF harvester at 0.35g (top) and 0.5g (bottom)

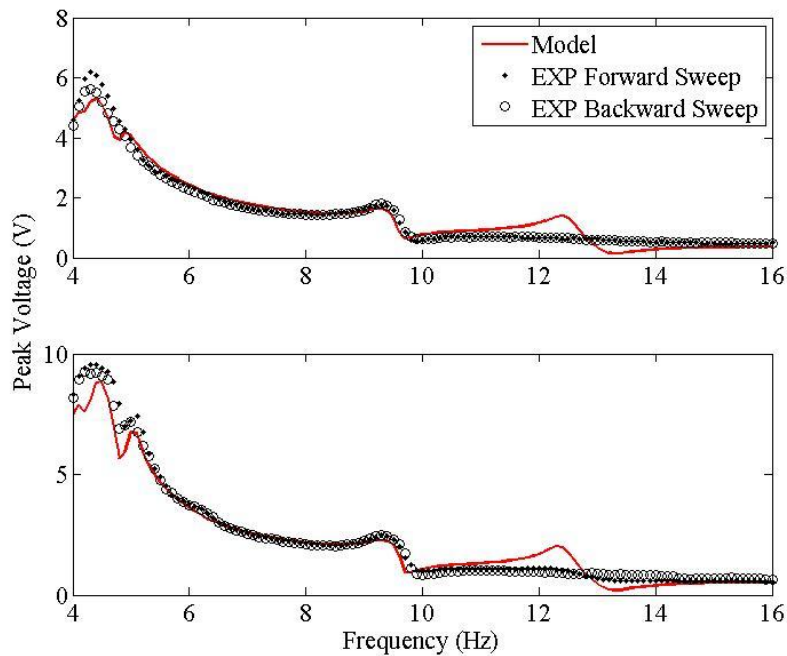


Figure 32 - Peak voltage comparison between the experimental results and the model for the middle magnet of the MDOF harvester at 0.35g (top) and 0.5g (bottom)

The model predictions for the middle magnet of the MDOF harvesters also compares well with the experimental results. In particular, the model captures the first two peaks at 4.2Hz and 9.5Hz. However, the model overestimates the third peak. The model also predicts slightly higher displacement at the main peak at 0.5g excitation level. One possible explanation is that the bottom spring reaches its full compression, resulting in lower displacement values for the middle magnet. This explanation is also support by the model prediction of the bottom magnet. Similar to the SDOF harvester, the predicted peak voltage is lower than the experimental data around the peak response frequencies, which gives further support to the theory that the actual radial flux is less than the predicted one.

In summary, both the SDOF and MDOF models compared well with the experimental results. The SDOF and MDOF prototypes are similar enough that some comparisons can be made between the two designs based on experimental results. As built, the SDOF and MDOF prototypes have a maximum power output of 39.7mW and 78.3mW respectively at 0.5g acceleration level. The MDOF prototype represents a 34.8% increase in power density over the SDOF prototype at their respective maximum power output. The MDOF design has additional degree of freedom which can be use for energy harvesting. The MDOF design has also increase

the power output of the middle magnet when compared to the SDOF design. In addition, the energy harvesters are operating in the linear region, where bifurcation is not a factor. Thus, they are not limited by the direction of the frequency shift of the input vibration. With the maximum peak responses at 4.2Hz and 7Hz for SDOF and MDOF respectively, both energy harvester are well suited for harvesting energy from human motion. Lastly, the load voltage generated through electromagnetic induction is sufficiently high and is always above the 0.2V required for efficient passive rectification from AC voltage to DC voltage.

5.3 Bifurcation

Bifurcation is a characteristic of nonlinear systems. As mentioned previously, bifurcation is when multiple solutions exist for any single frequency. The solution that occurs at any frequency depends on the direction of the frequency sweep. For a spring hardening system where the backbone curve leans toward the right, the forward sweep would results in the larger amplitude of the two solutions. Although the base accelerations levels use in this study are insufficient to engage the system in nonlinear behaviours, they are nonetheless important for investigation. The model predictions for higher accelerations are presented in Figure 33 Figure 34 for SDOF and MDOF system respectively. It is shown that at 1.2g, the base acceleration is sufficient enough to engage the nonlinear behaviour.

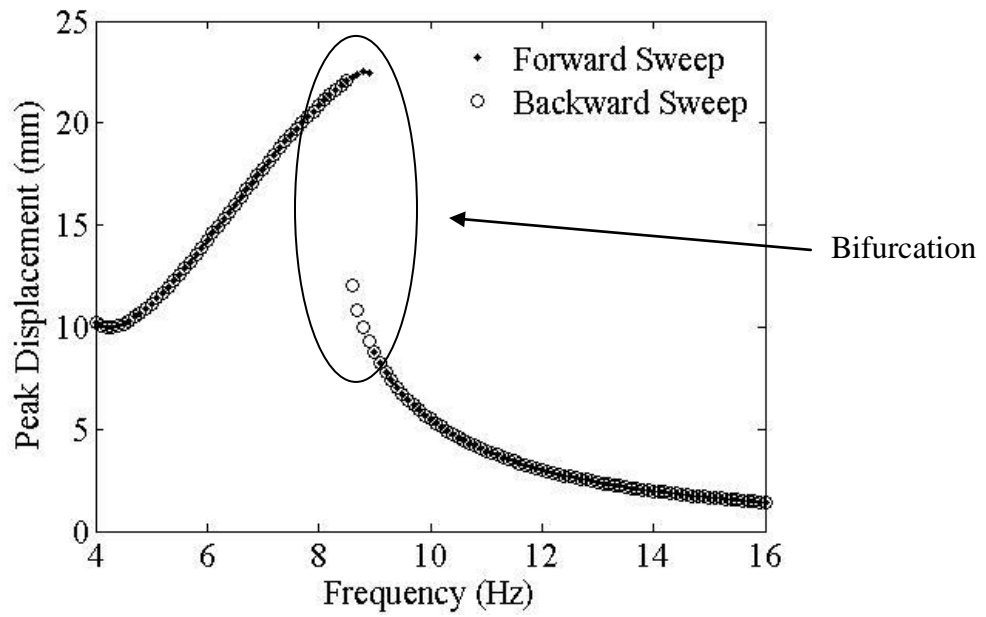


Figure 33 – Peak displacement vs. frequency graph by the model for the SODF harvester at 1.2g

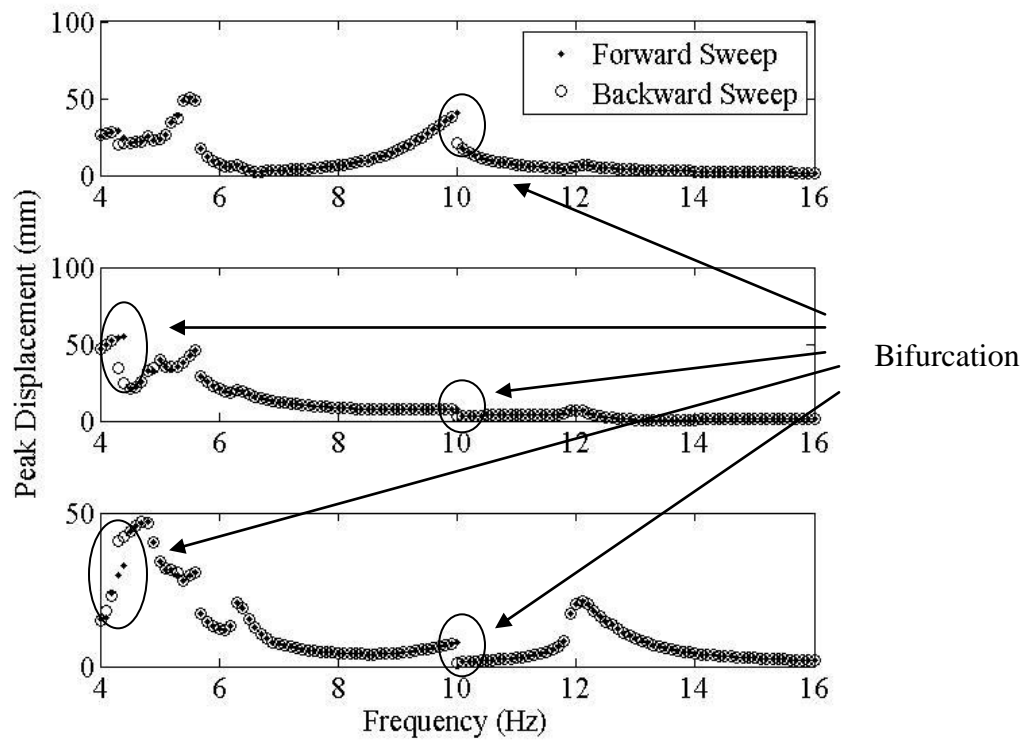


Figure 34 – Peak displacement vs. frequency graph by the model for the top, middle, and bottom magnets of the MODF harvester at 1.2g

For the SDOF system, the model predictions show a very prominent backbone curve (an asymmetric curve leaning towards the right), a characteristic of the spring hardening systems. The system clearly undergoes the bifurcation. Multiple solutions are clearly evident at the frequencies around 9 Hz. The results are also in good agreement with Mann and Sims [22], and Lee et al [23].

For the MDOF system, the model predicts bifurcation in all three magnets. The bifurcations occur in two different frequency ranges, one near the main peak at 4.3Hz and the other near the second peak at 10Hz. The multiple bifurcations are due to multiple degrees of freedom. There is no experimental verification of the bifurcation result for MDOF system due to infeasibility of this acceleration levels and the spring length limitations. However, the model predicts bifurcation for the MDOF at this acceleration at the frequencies around 4.3Hz and 9.9 Hz.

Chapter 6: Analysis of the Effect of Spring Stiffness

A study of the effect of the spring stiffness is performed on the MDOF energy harvester over the frequency range of 1 to 20 Hz because the SDOF harvester unit can be seen as a special case of the MDOF harvester where the stiffness of the top and bottom springs are infinitely large. Therefore, it is worthwhile to investigate what effect the spring stiffness would have the system. The effect of spring stiffness is found using the model developed in the previous sections.

6.1 Simulation Assumptions and Procedure

Since voltage directly correlates with power generation, i.e., $P(t) = \frac{V(t)^2}{R_{load}}$; to find the optimal power, the average peak voltage across the defined range of frequencies is maximized. In this part, the optimal stiffness values are found to serve this goal. All other parameters are fixed based on the following assumptions:

- a) The mechanical damping coefficients are based on the values determined by experimental testing for MDOF and SDOF devices, and assumed to be constant.
- b) The coil is offset by 0.5 inch from the equilibrium position of the middle magnet, where the magnetic flux density is the greatest for an axially magnetize magnet.
- c) The geometric distance is kept such that when the spring stiffness is infinite for the MDOF case, it matches geometry of the SDOF case.
- d) The spring stiffness is the same for the top and bottom springs
- e) The electric circuit used for the simulation is the same as the circuit used in the experiment
- f) The coil geometry is the same as the experiment

The harvesters are subjected to constant base acceleration of 0.35g and 0.5g, same as the experiment. The spring stiffness is varied between 10 N/m to 200 N/m. A very low spring stiffness value (i.e < 10 N/m) would not be feasible as they result in a fully compressed spring unless the spring has an infinitely large length, which is not a desirable design. The average peak voltage over the frequency spectrum is calculated from the frequency response curve using the developed model. The peak voltage response function is normalized with respect to the

frequency range (1 to 20 Hz) to find the average peak frequency. The parameters used for the model are shown in Table 5.

Table 5 – Parameter values used in the simulation for the SDOF and MDOF harvesters.

Parameters	SDOF	MDOF	Units
m_1	-	0.0125	kg
m/m_2	0.0267	0.0267	kg
m_3	-	0.0125	kg
c_{1m}	-	0.00287	-
c_m/c_{2m}	0.0956	0.144	-
c_{3m}	-	0.00287	-
LS_1	-	0.0254	m
LS_3	-	0.0254	m
h_1	-	0.0127	m
h/h_2	0.0254	0.0254	m
h_3	-	0.0127	m
L_s/L_m	0.0894	0.2037	m
l_{coil}	236.2	236.2	m
R_{load}	1000	1000	Ω
R_{coil}	845	845	Ω

6.2 Simulation Results

The results of the simulation study are shown in Figure 36 to Figure 38. In Figure 37 and Figure 38, the x-axis indicates the simulation case number and corresponding stiffness is shown in the legend. The spring stiffness affects the magnitude and the frequencies of the peaks. An increase in the spring stiffness increases frequency of the peak response and decrease the amplitude of the peak response. The frequency response of the MDOF harvester slowly approaches the frequency response of the SDOF harvester as spring stiffness increases. The frequency response of the MDOF harvester with spring stiffness of 200N/m converges to the SDOF harvester.

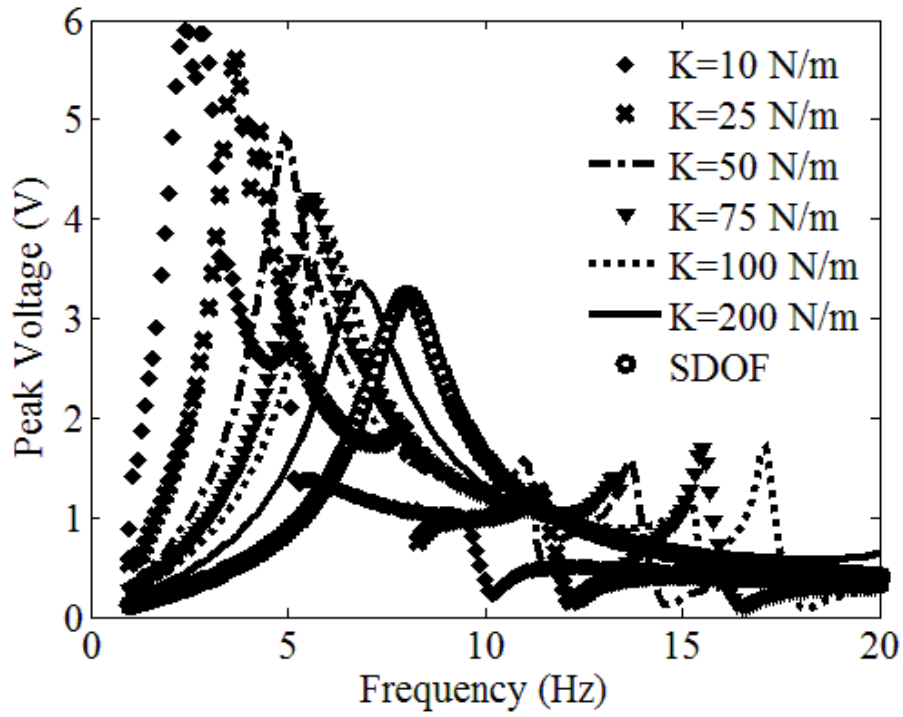


Figure 35 - Model peak voltage frequency response functions with different spring stiffness at 0.35g

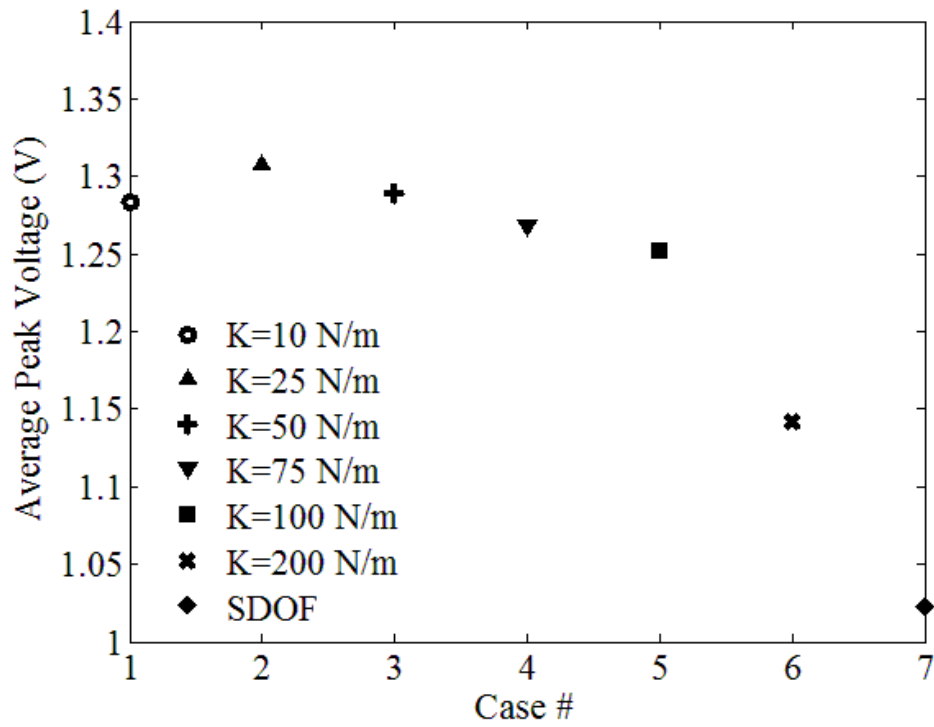


Figure 36 - Average peak voltage over the frequency spectrum (1-20Hz) for different spring stiffness at 0.35g

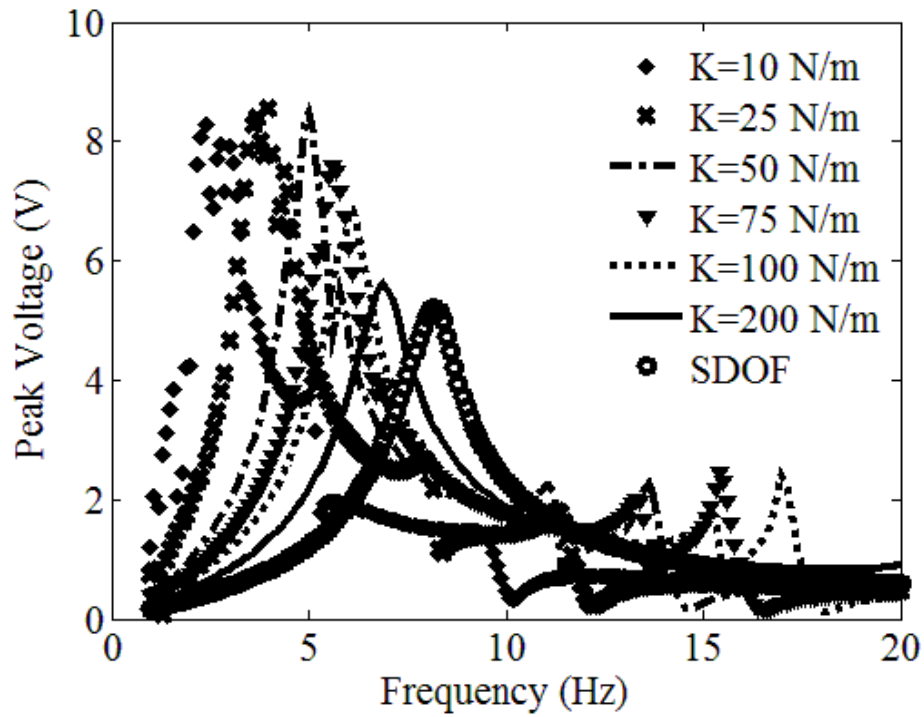


Figure 37 - Model peak voltage frequency response functions with different spring stiffness at 0.5g

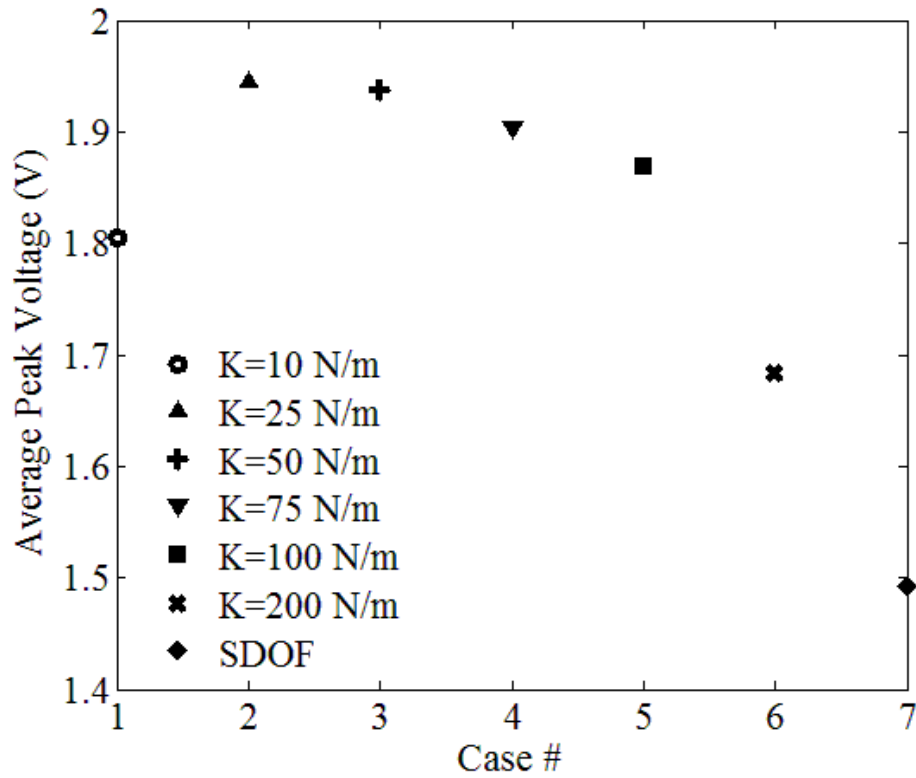


Figure 38 - Average peak voltage over the frequency spectrum (1-20Hz) for different spring stiffness at 0.5g

In general, the MDOF energy harvester has higher average peak voltage than the SDOF energy harvester. At 0.5g, the MDOF energy harvester has as much as a 30% increase in average peak voltage compared with the SDOF energy harvester. The spring stiffness that corresponds with the highest average peak voltage is 25 N/m for both 0.35g and 0.5g acceleration levels. However, a more rigorous analysis is required to determine what the optimal spring stiffness is. As mentioned previously, using a lower spring stiffness would result in a larger energy harvester due to the longer length of spring required to accommodate larger displacements. There is a tradeoff between power production and volume. Therefore, a power density analysis is required to determine the optimal spring stiffness.

This simulation demonstrates that the MDOF harvester has better power generating capabilities than the SDOF harvester solely based on the power generated by the middle magnet. The top and bottom magnets of the MDOF, which can also be used to harvest energy, have not been a factor in this simulation to make a fair comparison.

Chapter 7: Conclusion and Future Work

An electromagnetic MDOF energy harvester design was introduced. The MDOF design was a modification of a SDOF design in literature, and models were developed to predict the frequency response functions of the MDOF and SDOF harvesters. Subsequently, the SDOF and MDOF energy harvester prototypes were fabricated. A series of experiments were performed to characterize the magnetic force and the mechanical damping of the energy harvesters. The experimental frequency response functions of the prototypes were obtained using constant acceleration level sinusoidal sweep. Model results and experimental results were compared and analyzed. Based upon these results, the following conclusions could be made:

1. *The models showed good agreement with experimental results*

The SDOF and MDOF prototypes were subjected to a sinusoidal sweep with peak amplitudes of 0.35g and 0.5g. The experimental frequency response functions were compared with the model generated frequency response functions. Under both acceleration levels, the experimental displacement and voltage frequency response functions showed good agreement with the model predictions for both SDOF and MDOF energy harvesters.

2. *The energy harvester was operating in the linear region*

Forward (from low frequency to high frequency) and backward (from high frequency to low frequency) sinusoidal sweeps were performed on the SDOF and MDOF prototypes. The experimental frequency response functions were in agreement with the model predictions, where bifurcation did not occur (there was one single stable solution for all frequencies). Therefore, the energy harvesters were operating in the linear region.

3. *The MDOF prototype had a higher power density compared with the SDOF prototype*

Although the main peak of MDOF prototype is different compared with the SDOF prototype (4.2Hz vs. 7Hz), the MDOF prototype demonstrated it can produce greater power than the SDOF energy harvester at their respective main peaks. At 0.5g, the MDOF prototype had a 34.8% higher power density compared with the SDOF prototype.

4. *The MDOF harvester is suitable for harvesting energy using human motion and structural health monitoring applications*

The MDOF prototype has its main peak at 4.2Hz, which is in the frequency range required for human motion and structural health monitoring applications. Activities related to human motion such as walking and light jogging have shown to produce acceleration levels up to 1g, which is higher than the 0.35g and 0.5g used in the experiment. Some modifications can be made to the current prototypes to increase the performance for very lower acceleration levels in structural health monitoring applications.

5. *The model showed bifurcation does occur at higher acceleration levels*

The models showed given sufficient acceleration (approximately 1.2g), both SDOF and MDOF would bifurcate. This result was not confirmed experimentally due to the limitation of the prototypes.

6. *The energy harvester can use passive rectification*

The energy harvester prototypes demonstrated that passive rectification from AC to DC voltage could be used. Both the SDOF and MDOF energy harvesters are able to produce sufficient voltage ($>0.2V$) required throughout the entire tested frequency range (4-16Hz)

7. *The MDOF energy harvester had a higher average peak voltage than the SDOF harvester*

A study was performed to investigate the effect of spring stiffness. Besides changing the frequencies of the peaks, it also changed the magnitudes of the peaks. When normalized over the frequency range (1-20 Hz), the average peak voltage can be 30% higher when compared with the SDOF energy harvester at 0.5g. The spring stiffness that produced the highest average peak voltage was 25N/m. It should be noted again that using lower stiffness would result in a very large free spring length, which was not practical. A more rigorous power density analysis is required to compare the tradeoff between the increases in power production of using lower stiffness spring with the increase size of energy harvester to determine the optimal spring stiffness.

To date, the MDOF harvester design has only used the middle magnet to harvest energy, thus providing a direct comparison with the SDOF design. The next logical step is to build an electromagnetic MDOF energy harvester that harvest energy using all three magnets in order to take full advantage of the design. A parametric study, similar to the comparison between SDOF and MDOF harvester, should be performed. The goal of the study should be to maximize the total power production from all three magnets over the desired frequency range. In addition, new prototypes should be built such that bifurcation can be investigated experimentally.

Lastly, efforts should be made to miniaturize the size of the MDOF energy harvester. The current prototype is used to verify the validity of the design. For the ease of manufacturing, the prototype is made relatively large and may not be suitable for most energy harvesting applications. Further research is needed to explore smaller design options. It will be interesting to see if the MDOF design can be scaled down to the size of an AA battery.

References

- [1] Cook-Chennault, K.A., Thambi, N., and Sastry, A.M. (2008). Powering MEMS portable devices—a review of non-regenerative and regenerative power supply systems with special emphasis on piezoelectric energy harvesting systems. *Smart Materials and Structures*, 17, pp.043001 (33pp).
- [2] Roundy, S., and Wright, P.K. (2004). A piezoelectric vibration based generator for wireless electronics. *Smart Materials and Structures*, 13, pp.1131–1142.
- [3] Torah, R., Glynne-Jones, P., Tudor, M., O’Donnell, T., Roy, S., and Beeby, S.P. (2008). Self-powered autonomous wireless sensor node using vibration energy harvesting. *Measurement Science and Technology*, 19, pp.125202 (8pp).
- [4] Cheng, S. and Arnold, D.P. (2010). A study of a multi-pole magnetic generator for low-frequency vibrational energy harvesting. *Journal of Micromechanics and Microengineering*, 20, pp.025015 (10pp).
- [5] Anton, S.R and Sodano, H. (2007). A review of power harvesting using piezoelectric materials (2003–2006). *Smart Materials and Structures*, 16, pp.R1–R21.
- [6] Beeby, S P., Torah, R.N., Tudor, M.J., Glynne-Jones, P., O’Donnell, T., Saha, CR., and Roy, S. (2007). A micro electromagnetic generator for vibration energy harvesting. *Journal of Micromechanics and Microengineering*, 17, pp.1257–1265.
- [7] Sapinski, B. (2010). Vibration power generator for a linear MR damper. *Smart Materials and Structures*, 19, pp.105012 (12pp).
- [8] Zuo, L., Scully, B., Shetani, J. and Zhou, Y. (2010). Design and characterization of an electromagnetic energy harvester for vehicle suspensions. *Smart Materials and Structures*, 19, pp.045003 (10pp).
- [9] Yuen, S. Lee, J., Li, W.J., and Leong, P. (2007). “An AA-Sized vibration-based microgenerator for wireless sensor,” *IEEE Computer Society, PervasivEcomputing* Jan – March 2007, pp.64-72.
- [10] Elfrink, R., Renaud, M., Kamel, T.M., Nooijer, C de., Jambunathan, M., Goedbloed, M., Hohlfeld, D., Matova, S., Pop, V., Caballero, L., and Schaijk, R van. (2010). Vacuum-packaged piezoelectric vibration energy harvesters: damping contributions and autonomy for a wireless sensor system. *Journal of Micromechanics and Microengineering*, 20, pp.104001 (7pp).

- [11] Sari, I., Balkan, T., and Külah, H. (2010). An electromagnetic micro power generator for low-frequency environmental vibrations based on the frequency up-conversion technique. *Journal of Microelectromechanical Systems*, 19 (1), pp.14-27.
- [12] Shu, Y.C. and Lien, I.C. (2006). Analysis of power output for piezoelectric energy harvesting systems. *Smart Materials and Structures*, 15(6), pp.1499–1512.
- [13] Sodano, H.A., Inman, D.J. and Park, G. (2005). Generation and storage of electricity from power harvesting devices. *Journal of Intelligent Material Systems and Structures*, 16(1), pp.67–75.
- [14] Tadesse, Y., Zhang, S., and Priya, S. (2009). Multimodal energy harvesting system: piezoelectric and electromagnetic. *Journal of Intelligent Material Systems and Structures*, 20, pp.625-632.
- [15] Yang, B., Lee, C., Kee, W.L., and Lim, S.P. (2010). Hybrid energy harvester based on piezoelectric and electromagnetic mechanisms. *Journal of Micro/Nanolithography, MEMS and MOEMS*, 9 (2), pp.023002 (10pp).
- [16] Zhu, D., Roberts, S., Tudor, M.J., Beeby, S.P. (2010). Design and experimental characterization of a tunable vibration-based electromagnetic micro-generator. *Sensors and Actuators A*, 158, pp.284–293.
- [17] Wischke, M., Masur, M., Goldschmidtboeing F., and Woias, P. (2010). Electromagnetic vibration harvester with piezoelectrically tunable resonance frequency. *Journal of Micromechanics and Microengineering*, 20, pp.035025 (7pp).
- [18] Kovacic, I., and Brennan, M.J. (2011). *The Duffing Equation: Nonlinear Oscillators and their Behaviour*. John Wiley and Sons Ltd: Malaysia.
- [19] Erturk, A., Inman, D.J. (2011). Broadband piezoelectric power generator on high-energy orbits of the bistable Duffing oscillator with electromechanical coupling. *Journal of Sound and Vibration*, 330, pp.2339–2353.
- [20] Lin, J.T., and Alphenaar, B. (2010). Enhancement of energy harvested from a random vibration source by magnetic coupling of a piezoelectric cantilever. *Journal of Intelligent Material Systems and Structures*, 21, pp.1337-1341.

- [21] Stanton, S.C., McGehee, C.C., and Mann, B.P. (2010). Nonlinear dynamics for broadband energy harvesting: Investigation of a bistable piezoelectric inertial generator. *Physica D*, 239, pp.640-653.
- [22] Mann, B.P., Sims, N.D. (2009). Energy harvesting from the nonlinear oscillations of magnetic levitation. *Journal of Sound and Vibration*, 319, pp.515–530.
- [23] Lee, C., Stamp, D., Kapania, N.R., and Mur-Miranda, J.O. (2010). Harvesting vibration energy using nonlinear oscillations of an electromagnetic inductor. *Proceeding of SPIE 7683*, 76830Y, pp.1-12.
- [24] Saha, C.R., O'Donnell, T., Wang, N., and McCloskey, P. (2008). Electromagnetic generator for harvesting energy from human motion. *Sensors and Actuators A*, 147, pp.248–253.
- [25] Zhu, D., Tudor, M.J., and Beeby, S.P. (2010). Strategies for increasing the operating frequency range of vibration energy harvesters: a review. *Measurement Science and Technology*, 21, pp.022001 (29pp).
- [26] Chen, Y., and Salehian, A. (2012). Modeling, analysis and experimental validation of an electromagnetic energy harvesting unit. *Proceeding of SMASIS 2012 Conference*.
- [27] Duffy, M. and Carroll, D. (2004). Electromagnetic generators for power harvesting. *Proceeding of IEEE Power Electronic Specialists Conference*, 3, pp.2075-2081.
- [28] nPower PEG. [online] Available at: <http://www.npowerpeg.com/> [assessed August 18, 2012]
- [29] Galchev, T.V., McCullagh, J., Peterson, R.L., and Najafi, K. (2011). Harvesting traffic-induced vibrations for structural health monitoring of bridges. *Journal of Micromechanics and Microengineering*, 21(10), pp.104005 (13pp).
- [30] Sazonov, E., Li, H., Curry, D., and Pillay, P. (2009). Self-Powered sensors for monitoring of highway bridges. *IEEE Sensors Journal*, 9, pp.1422-1429.
- [31] Wang, Z., Wang, B., Wang, M., Zhang, H., and Huang, W. (2010). Model and experimental study of permanent magnet vibration-to-electrical power generator. *IEEE Transactions On Applied Superconductivity*, 20, pp.1110-1113.
- [32] Sheng, S., Wang, N., and Arnold, D.P. (2007). Modeling of magnetic vibrational energy harvesters using equivalent circuit representations. *Journal of Micromechanics and Microengineering*, 17, pp.2328-2335.

- [33] COMSOL (2008). *COMSOL Multiphysics Modeling Guide*. Burlington, MA.
- [34] K&J Magnetics. [online] Available at:
<http://www.kjmagnetics.com/proddetail.asp?prod=R84X0> [accessed June 29, 2012]
- [35] LMS (2007). *LMS SCADAS Mobile User and Installation Manual*, LMS Instruments: Leuven, Belgium.
- [36] LMS (2007). *The LMS Test.Lab Sine Control Manual*. LMS Instruments: Leuven, Belgium.
- [37] Inman, D.J (2008). *Engineering Vibration: Third Edition*. Pearson Education Inc: Toronto Canada.
- [38] Ramlan, R., Brennan M.J., Mace, B.R., and Kovacic, I. (2010). Potential benefits of a non-linear stiffness in an energy harvesting device. *Nonlinear Dynamics*, 59, pp.545-558.

Appendix A: MDOF Model Code

Below is a sample of the MDOF model code. The code is contained in two parts. The first part is a function, which contains the derived equation of motion. The second part is a program, which performs the sinusoidal sweep across the frequencies. The program accepts the parameters of the system, the start and end frequencies, the number of frequency point of interest, and the initial conditions of the system. The program calls a numerical solver ODE 45, utilizing the EOM contained function at each frequency of interest. It outputs the peak displacement, peak velocity and peak load voltage frequency response curves of the system.

```
function v=EOM_MDOF(T,Y)

global c_damp1 c_damp3 g b2dot k1 k3 m1 m2 m3 L_coil Rload Rcoil

z1 = Y(1);
zdot1 = Y(2);
z2 = Y(3);
zdot2 = Y(4);
z3 = Y(5);
zdot3 = Y(6);
omega = Y(7);

%magnetic force coefficients
a=20.38;
b=-288.9;
c=7.049;
d=-98.55;

%harvester geometric constants
L_harvester=0.2037-(0/1000);%[m] - length of energy harvester minus end stop
h1=(1*25.4)/1000;           %[m] - height of top magnet
h2=(1*25.4)/1000;           %[m] - height of middle magnet
h3=(1*25.4)/1000;           %[m] - height of bottom magnet
LS1=(1.25*25.4)/1000;       %[m] - free length of top spring
LS3=(1.25*25.4)/1000;       %[m] - free length of bottom spring

%magnetic flux coefficients
a1 = 0.04785;
b1 = 62.87;
c1 = 9.314e-006;
a2 = 0.04399;
b2 = 125.6;
c2 = 8.007e-006;
a3 = 0.01886;
b3 = 188;
c3 = 1.593e-005;
a4 = 0.006143;
b4 = 314.1;
c4 = -3.142;
a5 = 0.00394;
b5 = 376.9;
c5 = -3.142;
a6 = 0.0008607;
```

```

b6 =      256.3;
c6 =      3.141;
a7 =    0.0009059;
b7 =      628.3;
c7 =      3.142;
a8 =    0.0006762;
b8 =      439.8;
c8 =     -3.142;

%mechanical damping
c2_mech= 0.144;

%exponential forcing function
St=z1-z2-((h1+h2)/2); %distance between middle magnet and top magnet
Sb=z2-z3-((h2+h3)/2); %distance between middle magnet and bottom magnet

Ft=a*exp(b*St)+c*exp(d*St); %force between middle magnet and top magnet
Fb=a*exp(b*Sb)+c*exp(d*Sb); %force between middle magnet and bottom magnet

%finding electrical damping coefficient for middle magnet
pos = z2-0.10185; %finding relative position
Bavg =
a1*sin(b1*pos+c1)+a2*sin(b2*pos+c2)+a3*sin(b3*pos+c3)+a4*sin(b4*pos+c4)+a5*si
n(b5*pos+c5)+a6*sin(b6*pos+c6)+a7*sin(b7*pos+c7)+a8*sin(b8*pos+c8);

c2_elec=((Bavg*L_coil)^2)/(Rload+Rcoil); %calculating electrical damping
coefficient

c2_total=c2_elec+c2_mech; %summation of electrical and mechanical damping
coefficient

%EOM
v=[zdot1; -(c_damp1/m1)*zdot1+(k1/m1)*(-z1+L_harvester-LS1-0.5*h1)+(Ft/m1)-
g+b2dot*sin(omega*T);
zdot2; (Fb-Ft)/m2-(c2_total/m2)*zdot2-g+b2dot*sin(omega*T);
zdot3; -(c_damp3/m3)*zdot3+(k3/m3)*(-z3+LS3+0.5*h3)-(Fb/m3)-
g+b2dot*sin(omega*T);
0];

return

```

```

%THREE DEGREE OF FREEDOM MODEL
%YAN CHEN
%June 28, 2012

clear all
clc
close all

%declaring variables
global c_damp1 c_damp3 g b2dot k1 k3 m1 m2 m3 L_coil Rload Rcoil

%mass

```

```

m1=0.0125;           %[kg]
m2=0.0267;
m3=0.0125;

%spring constants
k1=35;               %[N/m]
k3=35;

%damping
c_damp1=0.0287;
c_damp3=0.0287;

%accelerations
g=9.81;              %[m/s^2]
b2dot=0.35*9.81;

%sweep frequency
np=121;               %number of points
f=linspace(4,16,np); %sweep frequency in Hz
omega=2*pi*f;         %convert to rad/s

%coil length
L_coil=236.2;        %[m]

%Resistances
Rcoil =845;           %[ohm]
Rload=1000;

%magnetic flux coefficients
a1 =    0.04785;
b1 =    62.87;
c1 =   9.314e-006;
a2 =    0.04399;
b2 =   125.6;
c2 =   8.007e-006;
a3 =    0.01886;
b3 =   188;
c3 =   1.593e-005;
a4 =    0.006143;
b4 =   314.1;
c4 =   -3.142;
a5 =    0.00394;
b5 =   376.9;
c5 =   -3.142;
a6 =   0.0008607;
b6 =   256.3;
c6 =    3.141;
a7 =   0.0009059;
b7 =   628.3;
c7 =    3.142;
a8 =   0.0006762;
b8 =   439.8;
c8 =   -3.142;

%-----%
% sweep

```

```

%initial conditions: displacement [m] and velocity [m/s]
z1new(1)=0.15925;
zdot1new(1)=0;
z2new(1)=0.10185;
zdot2new(1)=0;
z3new(1)=0.04445;
zdot3new(1)=0;

%time definition
t0 = 0;
tend = 40;
tsample = 10;
ts = [t0 tend];

for i=1:length(omega)

xo = [z1new(i); zdot1new(i); z2new(i); zdot2new(i); z3new(i); zdot3new(i);
omega(i)];

%call solver
[T,Z]=ode45(@EOM_MDOF, ts, xo);

%calculate voltage
    for count = 1:length(Z);
        z=Z(count,3)-0.10185;
        Bavg=
a1*sin(b1*z+c1)+a2*sin(b2*z+c2)+a3*sin(b3*z+c3)+a4*sin(b4*z+c4)+a5*sin(b5*z+c
5)+a6*sin(b6*z+c6)+a7*sin(b7*z+c7)+a8*sin(b8*z+c8);
        Z(count,8)=Bavg*L_coil*Z(count,4);
    end

%find average peak values
sample = round(length(Z)*(tend-tsample)/tend);

% %FIND PEAK VELOCITIES
% %for top
% upper_pks_f1_vel = findpeaks(Z(sample:length(Z),2),'minpeakdistance',53);
% lower_pks_f1_vel = findpeaks(-Z(sample:length(Z),2),'minpeakdistance',53);
% pk2pk_vel_f1(i) = mean(upper_pks_f1_vel) + mean(lower_pks_f1_vel);
%
%
% %for middle
% upper_pks_f2_vel = findpeaks(Z(sample:length(Z),4),'minpeakdistance',53);
% lower_pks_f2_vel = findpeaks(-Z(sample:length(Z),4),'minpeakdistance',53);
% pk2pk_vel_f2(i) = mean(upper_pks_f2_vel) + mean(lower_pks_f2_vel);
%
%
% %for bottom
% upper_pks_f3_vel = findpeaks(Z(sample:length(Z),6),'minpeakdistance',53);
% lower_pks_f3_vel = findpeaks(-Z(sample:length(Z),6),'minpeakdistance',53);
% pk2pk_vel_f3(i) = mean(upper_pks_f3_vel) + mean(lower_pks_f3_vel);

%FIND PEAK DISPLACEMENTS
%for top

```

```

upper_pks_f1_disp = findpeaks(Z(sample:length(Z),1),'minpeakdistance',53);
lower_pks_f1_disp = findpeaks(-Z(sample:length(Z),1),'minpeakdistance',53);
pk2pk_disp_f1(i) = mean(upper_pks_f1_disp) + mean(lower_pks_f1_disp);

%for middle
upper_pks_f2_disp = findpeaks(Z(sample:length(Z),3),'minpeakdistance',53);
lower_pks_f2_disp = findpeaks(-Z(sample:length(Z),3),'minpeakdistance',53);
pk2pk_disp_f2(i) = mean(upper_pks_f2_disp) + mean(lower_pks_f2_disp);

%for bottom
upper_pks_f3_disp = findpeaks(Z(sample:length(Z),5),'minpeakdistance',53);
lower_pks_f3_disp = findpeaks(-Z(sample:length(Z),5),'minpeakdistance',53);
pk2pk_disp_f3(i) = mean(upper_pks_f3_disp) + mean(lower_pks_f3_disp);

%FIND PEAK LOAD VOLTAGE
upper_pks_volt = findpeaks(Z(sample:length(Z),8),'minpeakdistance',53);
lower_pks_volt = findpeaks(-Z(sample:length(Z),8),'minpeakdistance',53);
pk_volt_load_f1(i) = ((mean(upper_pks_volt) +
mean(lower_pks_volt))/2)*(Rload/(Rload+Rcoil));

%find new initial conditions for next step
z1new(i+1)=Z(length(Z),1);
zdot1new(i+1)=Z(length(Z),2);
z2new(i+1)=Z(length(Z),3);
zdot2new(i+1)=Z(length(Z),4);
z3new(i+1)=Z(length(Z),5);
zdot3new(i+1)=Z(length(Z),6);
end

%plot results
% %velocities
% subplot(3,1,1);hold on
% plot(f,pk2pk_vel_f1*1000,'b');
% subplot(3,1,2);hold on
% plot(f,pk2pk_vel_f2*1000,'b');
% subplot(3,1,3);hold on
% plot(f,pk2pk_vel_f3*1000,'b');

%displacements
figure
subplot(3,1,1);hold on
plot(f,pk2pk_disp_f1*1000,'b');
subplot(3,1,2);hold on
plot(f,pk2pk_disp_f2*1000,'b');
subplot(3,1,3);hold on
plot(f,pk2pk_disp_f3*1000,'b');

%voltage
figure
plot(f,pk_volt_load_f1,'b');

```

Appendix B: SDOF Model Code

Below is a sample of the SDOF model code. Similar to the MDOF, the code is contained in two parts. The first part is a function, which contains the derived equation of motion. The second part is a program, which performs the sinusoidal sweep across the frequencies. The program accepts the parameters of the system, the start and end frequencies, the number of frequency point of interest, and the initial conditions of the system. The program calls a numerical solver ODE 45, utilizing the EOM contained function at each frequency of interest. It outputs the peak displacement, peak velocity and peak load voltage frequency response curves of the system.

```
%SDOF EQUATION OF MOTION
function v=EOM_SDOF(T,Y)

global m g b2dot L Rload Rcoil

z = Y(1);
zdot = Y(2);
omega = Y(3);

%magnetic coefficients
a=20.38;
b=-288.9;
c=7.049;
d=-98.55;

%magnetic flux coefficients
a1 = 0.04785;
b1 = 62.87;
c1 = 9.314e-006;
a2 = 0.04399;
b2 = 125.6;
c2 = 8.007e-006;
a3 = 0.01886;
b3 = 188;
c3 = 1.593e-005;
a4 = 0.006143;
b4 = 314.1;
c4 = -3.142;
a5 = 0.00394;
b5 = 376.9;
c5 = -3.142;
a6 = 0.0008607;
b6 = 256.3;
c6 = 3.141;
a7 = 0.0009059;
b7 = 628.3;
c7 = 3.142;
a8 = 0.0006762;
b8 = 439.8;
c8 = -3.142;

%geometric constants
l=0.098; %[m] - length of energy harvester from face of bottom magnet to
```

```

face of top magnet
h=0.0254;    %[m] - height of middle magnet

%mechanical damping
c_mech=0.0956;

%exponential forcing function
St=(1/2)-z-(h/2); %distance between center magnet and top magnet
Sb=z+(1/2)-(h/2); %distance between center magnet and bottom magnet

Ft=a*exp(b*St)+c*exp(d*St); %force between center magnet and top magnet
Fb=a*exp(b*Sb)+c*exp(d*Sb); %force between center magnet and bottom magnet

%finding electrical damping coefficient
Bavg =
a1*sin(b1*z+c1)+a2*sin(b2*z+c2)+a3*sin(b3*z+c3)+a4*sin(b4*z+c4)+a5*sin(b5*z+c
5)+a6*sin(b6*z+c6)+a7*sin(b7*z+c7)+a8*sin(b8*z+c8);

c_elec=((Bavg*L)^2)/(Rload+Rcoil); %calculating electrical damping
coefficient

c_total=c_elec+c_mech; %summation of electrical and mechanical damping
coefficient

%EOM
v=[zdot; (Fb-Ft)/m - (c_total/m)*zdot-g+b2dot*sin(omega*T);
0;];

```

```

%SINGLE DEGREE OF FREEDOM MODEL
%YAN CHEN
%JUNE 28, 2012

clear all
clc
close all

%declaring variables
global m g b2dot L Rload Rcoil

%mass
m=0.0257;          %[kg]

%accelerations
g=9.81;            %[m/s^2]
b2dot=0.35*9.81;

%frequency sweep
np=121;           %number of points
f=linspace(4,16,np); %[Hz]
omega=2*pi*f;     %convert to rad/s

```

```

%Resistances
Rload=1000;           %[ohm]
Rcoil=845;

%time span
t0 = 0;
tend = 40;
tsample = 10;
ts = [t0 tend];

%coil length
L=236.2;             %[m]

%magnetic flux coefficients

%Bravg M=1.05e6 NEW
a1 = 0.04785;
b1 = 62.87;
c1 = 9.314e-006;
a2 = 0.04399;
b2 = 125.6;
c2 = 8.007e-006;
a3 = 0.01886;
b3 = 188;
c3 = 1.593e-005;
a4 = 0.006143;
b4 = 314.1;
c4 = -3.142;
a5 = 0.00394;
b5 = 376.9;
c5 = -3.142;
a6 = 0.0008607;
b6 = 256.3;
c6 = 3.141;
a7 = 0.0009059;
b7 = 628.3;
c7 = 3.142;
a8 = 0.0006762;
b8 = 439.8;
c8 = -3.142;

%-----%
% sweep

%initial condition
xnew(1)=0;
xdotnew(1)=0;

for i=1:length(omega);

xo = [xnew(i); xdotnew(i); omega(i)];

%call solver
[T,Z]=ode45(@EOM_SDOF, ts, xo);

```

```

%calculate voltage
for count = 1:length(Z);
    z=Z(count,1);
    Bavg=
a1*sin(b1*z+c1)+a2*sin(b2*z+c2)+a3*sin(b3*z+c3)+a4*sin(b4*z+c4)+a5*sin(b5*z+c
5)+a6*sin(b6*z+c6)+a7*sin(b7*z+c7)+a8*sin(b8*z+c8);
    Z(count,4)=Bavg*L*Z(count,2);
end

sample = round(length(Z)*(tend-tsample)/tend);

%find velocity
upper_pks_vel = findpeaks(Z(sample:length(Z),2));
lower_pks_vel = findpeaks(-Z(sample:length(Z),2));
pk2pk_vel_f1(i) = mean(upper_pks_vel) + mean(lower_pks_vel);

%find displacement
upper_pks_disp = findpeaks(Z(sample:length(Z),1));
lower_pks_disp = findpeaks(-Z(sample:length(Z),1));
pk2pk_disp_f1(i) = mean(upper_pks_disp) + mean(lower_pks_disp);

%find voltage
upper_pks_disp = findpeaks(Z(sample:length(Z),4), 'minpeakdistance',55);
lower_pks_disp = findpeaks(-Z(sample:length(Z),4), 'minpeakdistance',55);
pk_volt_f1(i) = ((mean(upper_pks_disp) + mean(lower_pks_disp))/2);
pk_volt_load_f1(i) = pk_volt_f1(i)*(Rload/(Rload+Rcoil));

xnew(i+1)=Z(length(Z),1);
xdotnew(i+1)=Z(length(Z),2);
end

%plot results
%plot velocity
plot(f,pk2pk_vel_f1*1000,'b');

%plot displacement
figure
plot(f,pk2pk_disp_f1*1000,'b');

%plot voltage
figure
plot(f,pk_volt_load_f1,'b');

```

Appendix C: Magnet Datasheet



Figure C1 – R848 rare earth magnet

Table C1 - R848 rare earth magnet specifications

Dimension	1/2" od x 1/4" id x 1/2" thick
Material	NdFeB, Grade N42
Plating	Ni-Cu-Ni (Nickel)
Magnetization Direction	Axial
Brmax	13,200 Gauss = 1.32 Tesla
Weight	9.05 g



Figure C2 - R84X0 rare earth magnet

Table C2 - R84X0 rare earth magnet specifications

Dimension	1/2" od x 1/4" id x 1" thick
Material	NdFeB, Grade N42
Plating	Ni-Cu-Ni (Nickel)
Magnetization Direction	Axial
Brmax	13,200 Gauss = 1.32 Tesla
Weight	18.1 g

Dytran 3035AG Accelerometer

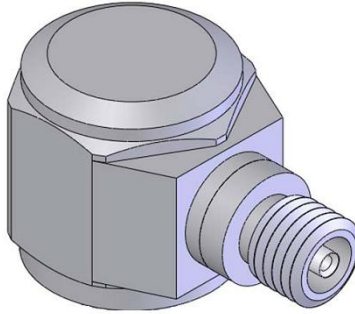


Figure D2 - Dytran 3035AG accelerometer

Table D3 – Dytran 3035AG accelerometer performance specifications

Sensitivity, $\pm 10\%$	100mV/g
Range F.S for $\pm 5V$ Output	± 50 g
Frequency Range	0.5 – 10000 Hz
Linearity	$\pm 1\%$ F.S

Table D4 – Dytran 3035AG accelerometer environmental specifications

Overload Limit	100mV/g
Temperature Range	-51 – 1649 °C

Table D5 – Dytran 3035AG accelerometer electrical specifications

Compliance Voltage Range	18 – 30 V
Supply Current	2 – 20 mA
Discharge Time Constant	0.5 Sec

Modal Shop 2075E Dual Purpose Shaker



Figure D3 – Modal Shop 2075E electromagnetic shaker

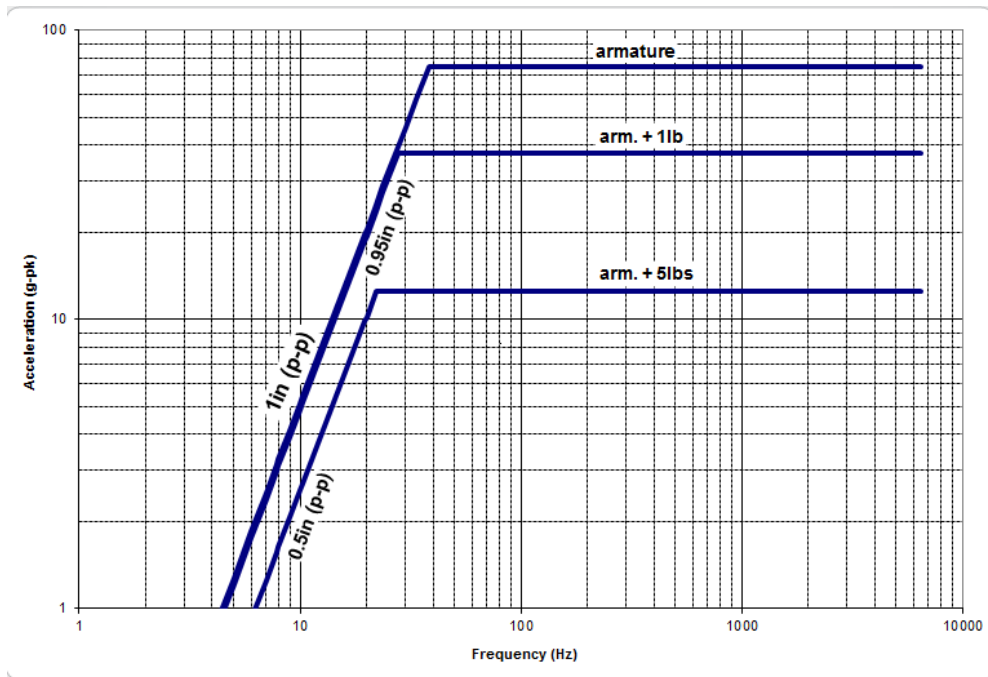


Figure D4 – Modal Shop 2075E electromagnetic shaker performance graph

Table D6 - Modal Shop 2075E electromagnetic shaker specifications

Force (sine peak)	334 N
Stroke (peak to peak)	25.4 mm
Frequency Range	DC – 6500 Hz
Max Payload	3.175 kg
Armature Weight	0.454 kg
Shaker Weight	16 kg

Chatillon DFX II Digital Force Gauge



Figure D5 – Chatillon DFX II digital force gauge

Table D7 - Chatillon DFX II digital force gauge specifications

Capacity	50 N
Accuracy	$\pm 0.3\%$ F.S
Data Sampling Rate	1000 Hz
Overload Protection	150% F.S
Instrument Weight	0.7 kg
Operating Temperature	4 – 43 °C

Appendix E: Additional Experiment Images



Figure E1 – Test structure

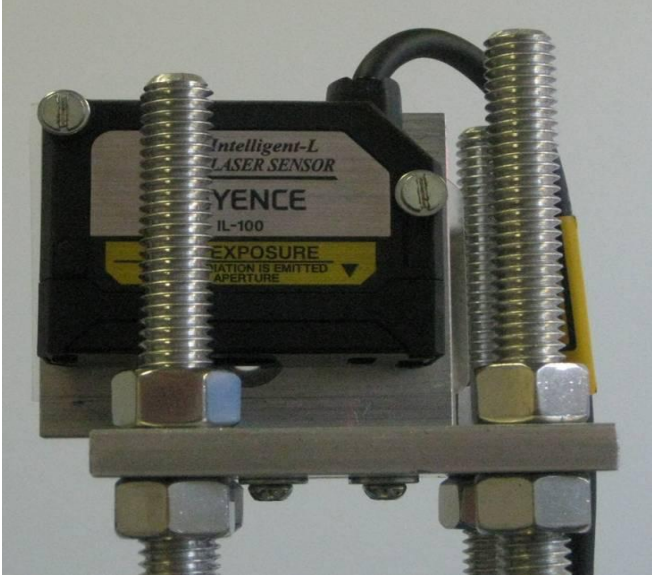


Figure E2– Keyence IL-100 laser sensor head on sensor mount on top of test structure



Figure E3 – Keyence IL-1000 laser sensor amplifier

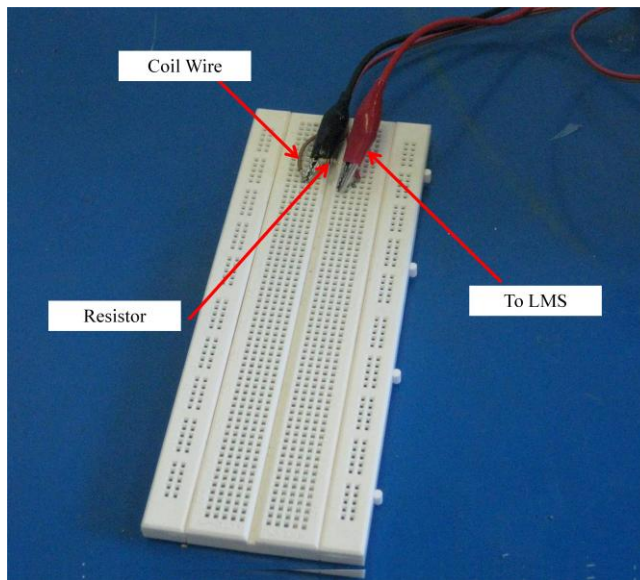


Figure E4– Electric for the energy harvester



Figure E5 – Exploded view of SDOF (top) and MDOF (bottom) prototypes